POLITECNICO
MILANO 1863

SCUOLA DI INGEGNERIA INDUSTRIALE
E DELL'INFORMAZIONE

Computational and Experimental Characterisation of Shear-Thinning Bioinks for Extrusion-based Bioprinting

TESI MAGISTRALE IN BIOMEDICAL ENGINEERING

Fattorini Letizia, 10678230

Advisor:
Silvia Bozzi

Co-advisors:
Alberto Cesare Luigi Redaelli

Justin Cooper-White

Academic year:
2025-26

Abstract: The growing shortage of transplantable organs, the rising clinical demand, and the risk of immune rejection from donor tissue have created an urgent need for alternative strategies. Bioprinting offers a promising route: by fabricating tissues and, ultimately, functional organs from the patient's own cells, it could provide patient-specific constructs that bypass rejection. The technology, however, still faces major limitations, chief among them reproducibility and reliability, production time and cost, and the high cell densities required for a functional construct. Overcoming them demands a deeper understanding of the physics governing bioink flow, where a central obstacle is the narrow biofabrication window: the conditions that preserve cell viability often compromise printing fidelity, and vice versa. This study addresses this need through a combined rheological and CFD characterisation of two widely used bioink precursors, hyaluronic acid (HA) and gelatin methacryloyl (GelMA), at two concentrations each (3%/6% and 5%/10% w/v); the lower-concentration formulations were additionally tested with encapsulated NIH 3T3 cells at high volume fraction (vf60). Rheological testing first established that all formulations are non-Newtonian and shear-thinning, a behaviour then described through the Cross, Carreau–Yasuda, and Power-law models to extract the constitutive parameters; this also revealed opposite responses to cell incorporation between the two materials (HA 3% and GelMA 5%). These parameters provided the input for CFD simulations in ANSYS Fluent, all reproducing the same converging nozzle geometry through three models: a microfluidic device (MFD), which is a 2.5D noodle-like geometry micro-PIV compatible, an axisymmetric, and a 3D, each enabling a distinct level of analysis and comparison. Predictions were validated against micro-PIV measurements on water, HA 3%, and GelMA 5%, with good agreement except for HA 3%, which revealed a clear discrepancy due to unexpected aggregation. The work establishes a reproducible rheological–computational–experimental pipeline, providing a methodological basis for future higher-concentration and cell-laden formulations.

Key-words: 3D bioprinting, shear-thinning bioink, cell-laden bioink, CFD, micro-PIV

1. Introduction

The shortage of donor organs remains a major challenge in transplant medicine. At the end of 2024, 13,570 patients were on active waiting lists within the Eurotransplant area, while only 7,160 organs from deceased donors were transplanted [1], highlighting a persistent mismatch between supply and demand. Moreover, allogeneic transplantation requires lifelong immunosuppressive therapy to prevent rejection, exposing recipients to infections, malignancies, and drug-related side effects. In this context, personalized regenerative medicine based on autologous cells has emerged as a promising alternative. The central idea is that 3D bioprinting technology could manufacture functional organs derived from a patient's own cells and extracellular matrix, in principle eliminating both the donor-availability problem and the issue of immune rejection, since the tissue would be genetically identical to the recipient [2], nowadays unfortunately printing fully functional solid organs is not yet an achievable goal with current technology [3]. Bioprinting has applications also extend to creating more realistic tissue and organ models for drug screening, disease modelling, and toxicity testing, often referred to as "organ-on-a-chip" systems when combined with microfluidics [4], for instance, a mini-liver or tumour model can be printed with multiple cell types to test drug toxicity or study cancer behaviour in an environment that better simulates the three-dimensional interactions of real tissue than a flat Petri dish culture [3].

3D bioprinting can be defined as a branch of additive manufacturing in which biomaterials, bioactive molecules, and living cells are deposited in a spatially controlled, layer-by-layer fashion to fabricate three-dimensional biological constructs [4]. The bioink constitutes the central material of the bioprinting process: a non-Newtonian suspension combining living cells with a polymeric precursor that acts as their carrier and structural matrix both during and after deposition [2]. For a bioink to be printable while remaining compatible with the cells it carries, it must satisfy a set of functional requirements that are often in tension with one another. More specifically, an ideal bioink should possess adequate mechanical, rheological, chemical, and biological properties: sufficient mechanical strength and shape fidelity after printing, tuneable gelation and stabilization kinetics, biocompatibility (and, where relevant, biodegradability) that mimics the native tissue microenvironment, and amenability to chemical modification to meet tissue-specific needs [5]. Rheologically, the bioink must exhibit shear-thinning behaviour, discussed more in detailed later, flowing readily under the shear forces generated within the nozzle while recovering sufficient viscosity at rest to preserve the printed shape [2]. It must also be capable of gelling or otherwise stabilizing shortly after deposition, transitioning from a printable liquid to a self-supporting solid through an appropriate crosslinking mechanism. Finally, it must remain biocompatible, providing an environment that does not compromise cell viability, adhesion, or downstream function [2]. Once gelled, most bioinks are hydrogels: three-dimensional polymeric networks capable of retaining large amounts of water while preserving structural integrity. Hydrogels offer several features that make them attractive as cell-laden matrices for bioprinting: most are biocompatible and biodegradable, and many possess intrinsic cell-binding sites that promote cell attachment, spreading, growth, and differentiation; some, in their chemically modified forms, can also be readily photo-crosslinked [5]. It is precisely this combination of high-water content together with the ability to sustain a defined structure, that makes hydrogels particularly suited to partially replicate the features of the native extracellular environment. Hydrogels can be classified according to the type of network that sustains them, they can be either chemical or physical. This distinction is relevant to bioprinting because it directly influences the long-term stability of the construct, its mechanical stiffness, and the extent to which it can be remodeled by the embedded cells. These ideal requirements are met differently by

the materials most used as bioink precursors, which include alginate, gelatin, collagen, fibrin/fibrinogen, gellan gum, hyaluronic acid, agarose, chitosan, and several synthetic polymers such as poly(ethylene glycol) (PEG) [5]. The present work focuses specifically on Hyaluronic acid (HA) and Gelatin Methacryloyl (GelMA) as bioink precursors, studied at concentrations of 3% and 6% (w/v) and of 5% and 10% (w/v), respectively, in cDMEM. The choice of these two materials is not incidental: HA and GelMA represent two distinct paradigms of polymeric network. The first one is a glycosaminoglycan naturally abundant in the extracellular matrix, it can form physical networks through chain entanglement and non-covalent inter-chain interactions even without chemical crosslinking, though its mechanical and rheological properties are frequently enhanced through chemical modification when used as a standalone bioink [3]. In contrast, GelMA forms chemical bonding relying on temperature and photo-crosslinking, in which UV exposure in the presence of a photo-initiator covalently bonds methacrylate groups grafted onto the gelatin backbone, yielding a network that, unlike unmodified gelatin, remains stable at physiological temperature [3]. This modification addresses a key limitation of unmodified gelatin, whose thermo-responsive (physical) gelation is typically slow and unstable, making covalent stabilization necessary for reliable shape retention after printing [5]. This fundamental structural difference is reflected in opposing rheological behaviours, both under static conditions and in the presence of embedded cells.

Three main printing modalities have been developed: droplet/inkjet- based bioprinting, which ejects discrete picolitre droplets of low-viscosity bioink through thermal or piezoelectric actuation; laser-assisted bioprinting, which uses pulsed laser energy to transfer bioink droplets from a donor slide without a physical nozzle, achieving high resolution and minimal mechanical stress on cells; and extrusion-based bioprinting, which continuously dispenses bioink through a nozzle as a filament [3]. A fourth, less widely adopted modality is stereolithography (SLA), a nozzle-free technique in which a liquid photosensitive polymer is selectively solidified layer-by-layer through laser-induced photopolymerization [2], Figure 1-1. Among these, extrusion-based bioprinting has become the most widely adopted modality in research, owing to a combination of practical advantages: relatively low equipment cost, compatibility with a broad range of bioink viscosities, ranging from dilute hydrogel solutions to dense, paste-like formulations, and the ability to print at high cell densities without the clogging issues that limit inkjet systems [3].

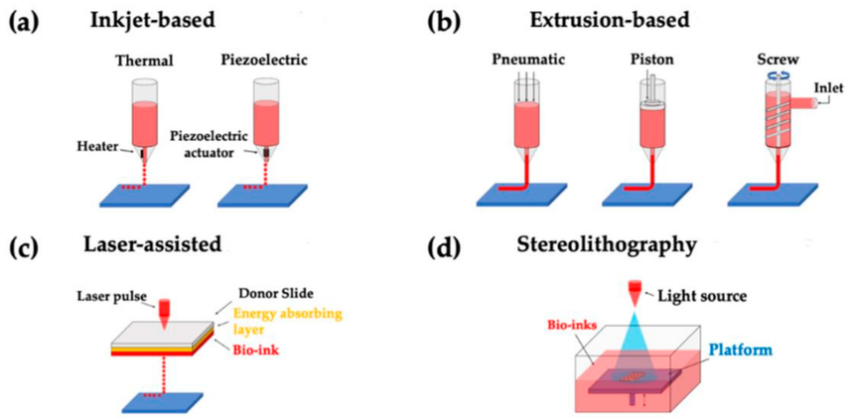

Figure 1-1: The four main bioprinting modalities: (a) inkjet-based (thermal and piezoelectric), (b) extrusion-based (pneumatic, piston, and screw), (c) laser-assisted, and (d) stereolithography. [6]

The bioink itself is typically a hydrogel which once deposited and crosslinked, it functions as the scaffold that physically supports the encapsulated cells during and after printing. This versatility,

however, has also disadvantages, since as the bioink-cell suspension is forced through the syringe and needle, cells are exposed to two distinct types of mechanical stress: shear stress, generated as the suspension flows along the needle wall, and extensional stress, generated by the abrupt velocity change as the flow converges through the needle's contractive region [7]. Both can rupture cell membranes and reduce post-printing viability; recent evidence indicates that extensional stress, although acting over a much shorter exposure time, can cause more acute damage than shear stress at the higher dispensing pressures typically required for viscous bioinks [7], Figure 1-2.

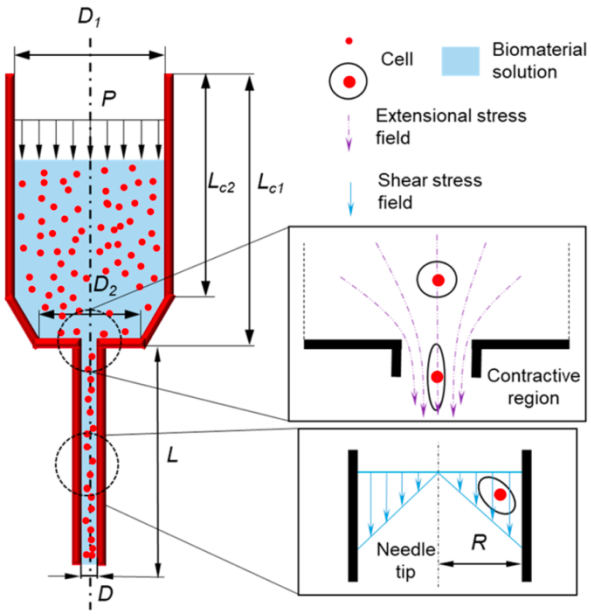

Figure 1-2: Schematic of extrusion-based bioprinting, showing cell exposure to extensional stress in the contractive region and shear stress at the needle tip. [7]

The degree of damage depends on printing parameters: dispensing pressure, needle diameter and length, and bioink rheology. Notably, this dependence also limits how densely cells can be packed within the bioink: since the magnitude of the shear stress is determined by multiplying the bioink's viscosity by the shear rate, any increase in cell concentration that raises bioink viscosity unavoidably increases the shear stress experienced during extrusion, thereby reducing post-printing cell viability [8]. As a result, extrusion-based bioprinting, despite its compatibility with highly viscous and concentrated bioinks compared to inkjet systems, typically yields a comparatively low post-printing cell viability, ranging from 40% to 80% [8]. Consequently, the cell density achievable in the printed construct remains far below physiological values, where tissue microenvironments reach approximately 3 – 5 x10^9 cells/ml. This tension between preserving cell viability and achieving physiological cell densities makes the relationship between print fidelity and cell survival a central design trade-off which is often summarized as the "narrow bio-fabrication window": the conditions that favour high printing resolution and shape fidelity (high pressure, small needle diameter) tend to be precisely those that maximize cell damage, while the conditions that preserve cell viability (low pressure, large needle diameter) compromise resolution. Reconciling these competing requirements remains an open methodological problem highlighting the necessity of focusing on the microfluidic characterization of flow behaviour within the extrusion needle itself, this will lead to ground bioprinting parameter selection in the underlying fluid dynamics, rather than a top-down approach starting from the target tissue architecture. Beyond the mechanical damage discussed above, the

presence of cells also alters the rheological behaviour of the bioink itself, with the direction of this effect depending on the concentration regime of the polymer precursor: in concentrated systems sustained by a physical network of inter-chain interactions, cell incorporation tends to reduce viscosity, whereas in dilute precursors lacking a consolidated network, cells behave as discrete particulate inclusions that increase resistance to flow, in a manner analogous to the Einstein model for dilute suspensions [9, 10], this will be discussed in more detail later.

To determine the rheological behaviour of a bioink itself, however, other factors besides cell content must also be taken into consideration, most fundamentally, how the precursor itself responds to shear. For an ideal-viscous (Newtonian) fluid, the shear viscosity η , defined as the ratio of shear stress τ to shear rate $\eta = \tau/\dot{\gamma}$, is a material constant: it remains independent of the shear rate applied, so that the flow curve $\tau(\dot{\gamma})$ is a straight line through the origin and the viscosity curve $\eta(\dot{\gamma})$ is flat [11]. Low-molecular liquids such as water, mineral oils, and blood plasma closely approximate this behaviour [11]. However, it should be noted that the majority of bioink precursors are polymer solutions whose viscosity changes with the applied shear rate. For this reason, they are classified as non-Newtonian fluids, more specifically, they exhibit shear-thinning behaviour. In this type of fluid, viscosity decreases as the shear rate increases: under shear, polymer chains progressively disentangle and align in the flow direction faster than they can re-entangle, lowering the resistance to flow [11]. This behaviour is precisely what allows a bioink to be extruded through a narrow nozzle, where shear rates are high, while still recovering sufficient viscosity at rest to retain the printed shape once deposited, consistent with the printability requirement discussed previously. To describe a complete flow or viscosity curve for a non-Newtonian fluid, several mathematical constitutive (model) functions have been developed; among the many models available, the present work focuses on the Power-law (Ostwald/de Waele), Cross, and Carreau-Yasuda models.

Direct experimental measurement of flow inside an extrusion needle is severely limited by scale and accessibility, as the relevant length scales are too small and the geometry too enclosed for most measuring instruments to be inserted without disturbing the flow itself [12]. Computational fluid dynamics (CFD) offers an alternative: by numerically solving the governing flow equations, it provides full-field access to velocity, shear stress, and pressure throughout the domain, including at locations not directly measurable [12]. Within bioprinting specifically, CFD has become a key tool for testing printing parameters such as nozzle speed, shear stress, and cell viability without the cost and time required for repeated physical trials, and has been used in particular to study how nozzle geometry and operating pressure govern the shear stress experienced by cells as they pass through the needle [13]. For an incompressible Newtonian fluid, this flow is governed by the continuity and momentum (Navier–Stokes) equations, whose relative importance of viscous versus inertial forces is captured by the dimensionless Reynolds number, $\mathrm{Re} = \rho v_0 L_0/\mu$ [12]. The same framework applies to non-Newtonian fluids such as the bioink precursors considered here, with the difference that viscosity can no longer be imposed as constant but must instead be defined as a function of the local shear rate [12]. At the low Reynolds numbers and small length scales characteristic of bioprinting needles, the flow is expected to be laminar, which makes a fully developed, axisymmetric velocity profile (Poiseuille flow) a natural theoretical reference for the CFD results. CFD models, however accurate in their underlying assumptions, require experimental validation to be considered predictive of the real flow behaviour. For this type of bioprinting study, the common approach involves a CFD simulation followed by an experimental validation, which can be either qualitative or quantitative. Qualitative validation is typically carried out through streak imaging, a technique that visualises flow lines by continuously illuminating fluorescent particles dispersed within the

fluid, making patterns such as vortices, bifurcations, or flow instabilities directly observable [14]. However, streak imaging does not allow for a direct quantitative comparison between the velocity profile predicted by CFD and the one observed experimentally: as noted in the Rodd's work [14], in unstable flow regimes it becomes difficult to characterise the vortex mechanism from streak image analysis alone, due to the high frequency of oscillations in the flow structure and the three-dimensional nature of the flow. Quantitative validation, on the other hand, is carried out through micro-Particle Image Velocimetry (micro-PIV), as is done in the present work. The technique relies on acquiring two successive frames of the flow field, each captured during a short laser pulse, with the fluid seeded with micron-sized tracer particles. Each image is divided into small sub-regions, called interrogation areas; for each of these, the displacement of particles between the first and second frame is determined through pixel-by-pixel cross-correlation between the two images, identifying the correlation peak that corresponds to the most probable particle displacement. Knowing the time interval between the two pulses and the displacement measured within each interrogation area, which is converted into a local velocity vector, allows to create a complete vector map of the flow field over the entire area of interest [15]. Unlike streak imaging, micro-PIV therefore provides a pointwise numerical value that can be directly compared against the velocity profile predicted by the CFD simulation, allowing for a rigorous validation of the computational predictions.

This study pursues two complementary objectives. The first is the rheological characterisation of HA and GelMA bioink precursors, both in the absence and in the presence of encapsulated cells, to obtain the constitutive parameters required to describe their non-Newtonian flow behaviour and to serve as input for the CFD simulations implemented in ANSYS Fluent. Beyond providing these parameters, this characterisation aims to clarify how the incorporation of cells at high volume fraction alters the underlying rheological response of each material, an effect that, as discussed above, manifests in opposite directions for HA and GelMA depending on the presence and nature of their respective network structures. The second objective is the development of a CFD model of the microfluidic device (MFD) designed to mimic the geometry of a bioprinting nozzle, together with its quantitative experimental validation against micro-PIV measurements performed on acellular fluids (water, HA 3%, and GelMA 5%) for which direct optical access to the flow field was experimentally feasible. Taken together, these two objectives converge toward a broader aim: to advance the understanding of the flow behaviour of conventional shear-thinning hydrogels under conditions relevant to extrusion-based bioprinting, by jointly characterising their rheology and their fluid dynamics, and by examining how the device geometry shapes their flow behaviour at the channel scale. Building on the existing MFD design and extending it through the axisymmetric and 3D computational models developed in this work, together with their quantitative experimental validation, this study aims to provide a more refined physical understanding of bioink flow, which may turn into improvements in process conditions, device geometry, and bioink characteristics that ultimately lead to better bioprinting performance.

2. Materials and Methods

2.1 Microfluidic Device (MFD)

The microfluidic device was fabricated in polydimethylsiloxane (PDMS) using standard soft lithography techniques with SU-8 photoresist molds at the Queensland node of the Australian National Fabrication Facility (ANFF-Q), The University of Queensland, Figure 2-1. The PDMS layer was bonded to a glass slide through oxygen plasma treatment. An inlet tubing system was connected

to allow injection of the fluid samples into the device, while a reservoir was carved at the outlet end to collect the extruded gel exiting the microfluidic geometry.

Figure 2-1: PDMS microfluidic device fabricated via soft lithography and bonded to a glass slide. An inlet tube allows fluid injection into the channel, and a collection well at the outlet retains the expelled gel and fluid.

The geometry of the microfluidic device was reconstructed from a two-dimensional cross-sectional profile (Figure 2-2), representing the planar layout of the device with overall dimensions of 30.36 mm in length and 8.8 mm in width, featuring a converging nozzle geometry designed to replicate the tip of a bioprinting needle. The channel has a uniform depth of 50 µm, resulting in a rectangular cross-section of 8.8 mm × 50 µm at the inlet.

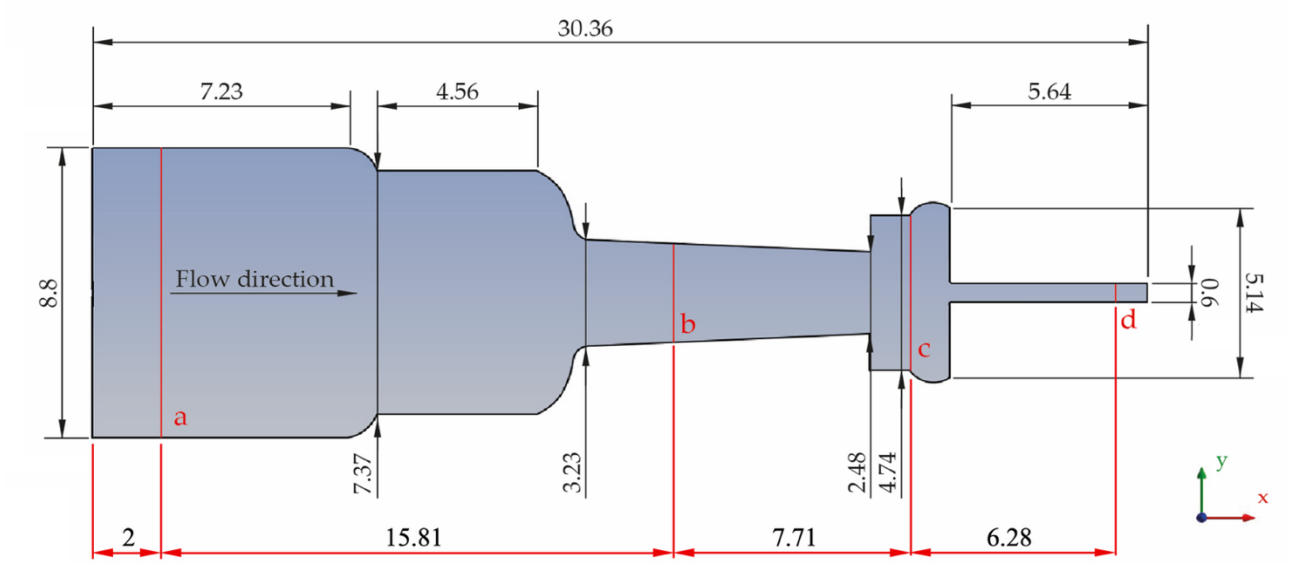

Figure 2-2: Microfluidic device geometry with dimensions in mm. Red lines indicate the four cross-sections (a, b, c, d) selected for velocity and wall shear stress evaluation.

2.2 Preparation of hydrogel precursor solutions and cell-laden bioinks

All solutions were prepared using complete Dulbecco's Modified Eagle Medium (cDMEM) as solvent, consisting of 90% high-glucose DMEM, 10% fetal bovine serum (FBS), and 1% penicillin/streptomycin (Pen/Strep, Thermo Fisher Scientific, Waltham, MA, USA).

Hyaluronic acid (HA) solutions at 3% and 6% (w/v) were prepared by dissolving HA powder (200 kDa, Lifecore Biomedical Inc., Chaska, MN, USA) in cDMEM at the appropriate mass-to-volume ratio. The powder was wetted using a vortex mixer and left on a roller overnight to ensure complete dissolution, then stored at 4°C until use.

GelMA solutions at 5% and 10% (w/v) were prepared by dissolving lyophilized type A GelMA (degree of functionalization ~80%, Gelomics Pty Ltd, Brisbane, Australia) in cDMEM at the appropriate mass-to-volume ratio. The powder was initially wetted using a vortex mixer, then placed in a water bath at 37°C overnight to ensure complete dissolution. Complete dissolution was confirmed by the absence of visible aggregates and by homogeneous flow upon gentle tilting. Solutions were stored at 4°C in the dark until use. Before the use, all solutions are heated in a water bath at 37°C.

NIH 3T3 fibroblast cells (ATCC, CRL-1658) were incorporated into the HA 3% and GelMA 5% solutions at a target volume fraction of 60% (vf60), selected to simulate a high cell density condition representative of dense biological tissues. Cells were cultured in cDMEM and detached from T-flasks using TrypLE (Thermo Fisher Scientific) following standard protocols. Cell concentration was determined by Trypan Blue exclusion (1:1 dilution) using an automated haemocytometer. Cells were centrifuged at 300 rcf for 5 minutes, the supernatant was removed, and the pellet was resuspended in cDMEM to obtain a final concentration of 10^8 cells/mL (corresponding to vf60). The actual cell volume fraction was measured by centrifuging the suspension in calibrated capillaries at 300 rcf for 3 minutes and measuring the pellet height (H_{cell}) and total suspension height (H_{tot}) with a digital calliper.

2.3 Rheological Characterization

Rheological measurements were performed on all bioink precursors described above, using an AR-G2 rheometer (TA Instruments, New Castle, DE, USA) equipped with a Peltier plate and a 20 mm parallel plate geometry at a gap of 100 μm, Figure 2-3. All measurements were conducted at 22°C, and a solvent trap filled with paraffin oil was used to prevent solvent evaporation during testing. Three replicates were performed for each material. Steady-state shear rate sweep tests were conducted using a steady-state ramp from 1 to 2000 s^{-1} with 10 points per decade and an equilibration time of 1 minute per point. Sample preparation and conditioning protocols were optimized for each material to ensure reproducibility. For HA 3% and HA 6% solutions, samples were heated to 37°C for 10 minutes and then degassed under vacuum for 15 minutes prior to loading, to remove air bubbles and allow the fluid to equilibrate to room temperature. The conditioning step consisted of maintaining a constant temperature of 22°C for 5 minutes before measurement. For GelMA 5% and GelMA 10% solutions, samples were placed in a water bath at 37°C for 10 minutes, followed by vacuum degassing for 10 minutes, and then loaded directly onto the rheometer. A two-step conditioning protocol was applied: in the first step, the temperature was set to 37°C to facilitate sample loading; subsequently, the temperature was lowered to 22°C and maintained for 20 minutes to allow thermal equilibration. In the second conditioning step, a pre-shear of 2 Pa was applied at 22°C to erase the loading history and stabilize the material microstructure prior to measurement.

For HA 3% and GelMA 5%, the cellular formulations (vf60) were characterised following the same protocol as the acellular ones with three independent loading replicates at T = 22 °C.

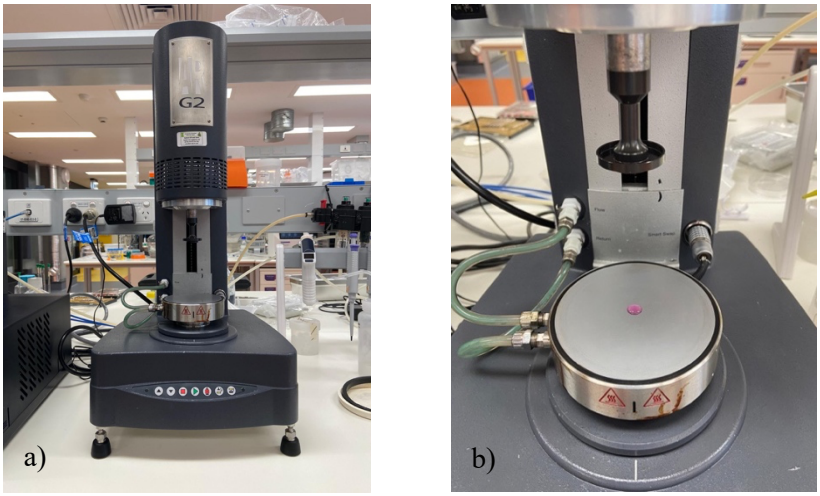

Figure 2-3: (a) AR-G2 rheometer (TA Instruments, New Castle, DE, USA) used for the rheological characterization of the hydrogel samples. (b) Hydrogel sample loaded onto the AR-G2 equipped with a Peltier plate and a 20 mm parallel plate geometry prior to testing.

The hydrogel precursors investigated in this work exhibit shear-thinning behaviour, meaning that their apparent viscosity decreases with increasing shear rate [11]. Because the viscosity of such materials is not constant but depends on the applied shear conditions, a single viscosity value is not sufficient to describe their flow behaviour; instead, the full viscosity-versus-shear-rate curve must be characterized and described through an appropriate constitutive model to be used as input for the CFD simulations. For each material, the three viscosity-versus-shear-rate curves obtained from the rheometer were averaged to produce a mean flow curve. The averaged viscosity–shear rate data were fitted in MATLAB using the Curve Fitter toolbox by comparing different constitutive models commonly adopted for shear-thinning fluids, like Cross, Carreau–Yasuda, Power-law, and Herschel–Bulkley models and others. Model selection was primarily based on the coefficient of determination (R^2), while also considering the ability of each model to describe the experimental trend over the investigated shear-rate range. The best-fitting constitutive model was then selected for each material and used as input for the CFD simulations.

2.4 Computational Fluid Dynamics Simulations

2.4.1 Geometries

CFD simulations were performed using ANSYS Workbench (Academic License, 2025 R1, ANSYS Inc., Canonsburg, PA, USA) to investigate the flow behaviour of bioink precursors within the microfluidic device.

The MFD computational model was developed to reproduce the geometry of the PDMS microfluidic device described above, which corresponds to a 2.5D noodle-like, micro-PIV-compatible geometry, with two symmetry planes applied to restrict the simulation domain to one quarter of the full geometry to reduce computational cost. Four cross-sections were defined at locations considered geometrically and fluid-dynamically significant, as shown in Figure 2-2 : section A, in the wide inlet region; section B, at the beginning of the contraction; section C, immediately downstream of the contraction; and section D, at the outlet of the narrow channel, corresponding to the nozzle tip position in a real bioprinting configuration. Section D represents the primary region of interest, as it is where the highest velocities and wall shear stresses are expected and where the material is

ultimately extruded. The MFD model was designed to enable direct comparison with the micro-PIV experimental measurements performed on the physical device.

The axisymmetric model simulates only a slice of the geometry and is computationally less expensive than the full 3D model, with a simplified mesh that reduces the likelihood of numerical instabilities. It was obtained by applying a symmetry condition along the x-axis of the 2D profile, retaining a two-dimensional planar domain that is assumed to be representative of the full circumferential distribution through the axisymmetric assumption.

The 3D model was generated by revolving the 2D profile 360° around the x-axis, producing a complete three-dimensional geometry with a circular cross-section. This model fully resolves the flow field without geometric simplifications and was used as a reference for comparison with the axisymmetric results. The axisymmetric and 3D models were compared to assess the computational consistency of the two approaches, as the axisymmetric solution should, by definition, converge to the 3D solution in the absence of asymmetric flow phenomena.

2.4.2 Mesh generation

The meshing of the MFD model was performed in two sequential steps to achieve simultaneous control over planar mesh refinement and boundary layer resolution in the height direction. In the first step, a structured 2D mesh was produced using the Fluent Meshing tool adopting a quad-dominant face meshing method. The planar geometry was subdivided into regions based on the local characteristic widths, and mesh density was progressively increased toward the contraction zone to adequately capture the flow gradients associated with the geometric narrowing. The resulting mesh was structured and continuous across all subdomains.

In the second step, the 2D mesh was imported into ICEM CFD, where a three-dimensional volume was obtained through a sweep extrusion along the height direction. To resolve the boundary layer developing at the top and bottom walls, a non-uniform node distribution based on a geometric progression was imposed along the extrusion direction. Ten layers were distributed over the 25 μm half-height of the channel, with a first layer height of 0.8 μm and a growth factor of 1.2375. A mesh independence study was conducted to verify that the selected element sizes did not significantly influence the simulation results; for further methodological details referred to the previous work [16]. Compared with the mesh described in the previous work, additional inflation layers were introduced along the lateral walls on the XY plane using the ANSYS Meshing inflation tool, with a smooth transition, a transition ratio of 0.272, a maximum of 3 layers, and a growth rate of 1.2. The final MFD mesh consisted of approximately 2.29 million elements and 2.08 million nodes.

The axisymmetric mesh was generated following the same approach used for the first step of the MFD model, adopting a quad-dominant face meshing method applied to the 2D planar geometry in ANSYS Meshing, with CFD physics preference and Fluent solver settings. Eight face sizing controls were applied across the domain to progressively refine the mesh in regions of geometric complexity, particularly in the contraction zone. Inflation layers were applied along the channel walls using the smooth transition inflation option, with a transition ratio of 0.272, a maximum of 2 layers, and a growth rate of 1.2. The final mesh consisted of 231,061 elements.

The 3D mesh was generated in ANSYS Meshing with CFD physics preference and Fluent solver settings. A patch-conforming method based on tetrahedral elements with quadratic element order was applied to the entire volume to control the element shape across the domain. Face sizing controls

were applied to refine the mesh in the contraction region, following the same refinement strategy adopted for the previous geometries. The final mesh consisted of 1,730,665 elements.

2.4.3 Simulation parameters and boundary conditions

All simulations were performed in ANSYS Fluent using a pressure-based solver. The flow was modelled as laminar, consistent with the very low Reynolds numbers characterizing the investigated conditions. All fluids were assumed to be incompressible, and the density was set equal to that of water. Water was modelled as a Newtonian fluid with constant viscosity, while the hydrogel precursors were described using the constitutive laws selected from the rheological characterization. The corresponding model parameters are reported in the Results Section 3.1.

A velocity-inlet condition was imposed at the inlet, a pressure-outlet condition with zero-gauge pressure at the outlet, and no-slip conditions were applied to the physical channel walls. Gradients were evaluated using the least-squares cell-based method, with second-order discretization schemes for pressure and momentum. Pressure–velocity coupling, initialization methods, inlet velocities, and convergence criteria were defined according to the specific geometry, as described below.

For the MFD geometry, a steady-state simulation was performed. Since the MFD has a rectangular cross-section, the inlet condition was defined by matching the inlet Reynolds number to that of a circular reference geometry with diameter $D = 8.8\,\text{mm}$, operating at the target flow rate of $Q = 0.5\,\text{mL/hr}$. The corresponding circular inlet velocity was $V_{circ} = 2.28 \times 10^{-6}$, yielding $Re \approx 0.020$ for water. Using the hydraulic diameter of the rectangular inlet ($D_h = 99.4\mu\text{m}$), the equivalent inlet velocity for the MFD model was $V_{rect} = 2.02 \times 10^{-4}\text{m/s}$, corresponding to an equivalent volumetric flow rate of approximately 0.32 mL/h. This velocity was applied to all simulated fluids. Two symmetry planes were applied, reducing the computational domain to one quarter of the full geometry. Standard initialization was used, with the x-velocity initialized to the inlet velocity and the remaining velocity components set to zero. Pressure–velocity coupling was handled using the SIMPLEC algorithm, and convergence was assessed using an absolute residual criterion of 1×10^{-5}.

For the axisymmetric model, a steady-state simulation was performed with the 2D space option set to axisymmetric. The inlet velocity was set to $2.28 \times 10^{-6}\text{m/s}$ to reproduce the target flow rate of 0.5 mL/h in the circular inlet section. Pressure–velocity coupling was handled using the SIMPLEC algorithm, convergence was assessed using an absolute residual criterion of 1×10^{-5}, and hybrid initialization was adopted.

For the 3D model, a transient formulation was adopted due to convergence difficulties encountered with the corresponding steady-state simulation. This approach improved numerical stability and allowed the flow field to progressively develop toward a stable solution. The inlet velocity was set to $2.28 \times 10^{-6}\text{m/s}$, corresponding to the target flow rate of 0.5 mL/h, with the same outlet and wall boundary conditions used for the axisymmetric model. Pressure–velocity coupling was handled using the SIMPLE algorithm, and standard initialization was computed from the inlet. Convergence at each time step was assessed using an absolute residual criterion of 1×10^{-4}. The time step was selected based on a Courant number of 1, using the maximum velocity in the domain ($u_{max} = 5 \times 10^{-4}\text{m/s}$) and the smallest cell size ($\Delta x_{min} = 5 \times 10^{-5}\text{m}$), resulting in $\Delta t = 0.1\text{s}$. The total simulated time was estimated from the device length and inlet velocity, giving a residence time of approximately $1.33 \times 10^{4}\text{s}$. Accordingly, the simulation was run for 133,500 time steps, with a maximum of 50 iterations per time step. All key simulation parameters are summarised for each model in Table 2-1.

Table 2-1: Summary of the main simulation parameters for the three computational models: MFD, axisymmetric, and 3D.

Model	Formulation	Re	Inlet condition	Inlet velocity	Outlet	Walls	Residual
MFD	Steady state	≈ 0.020	$Q_{eq} \approx 0.32$ mL/h	$2.02 \cdot 10^{-4}$ m/s	0 Pa	No-slip	$1 \cdot 10^{-5}$
Axisymmetric	Steady state	≈ 0.020	Q = 0.5 mL/h	$2.28 \cdot 10^{-6}$ m/s	0 Pa	No-slip	$1 \cdot 10^{-5}$
3D	Transient	≈ 0.020	Q = 0.5 mL/h	$2.28 \cdot 10^{-6}$ m/s	0 Pa	No-slip	$1 \cdot 10^{-4}$

2.5 Micro-Particle Image Velocimetry (Micro-PIV)

2.5.1 Experimental Setup

Micro-PIV measurements were performed using an all-in-one 2D2C MicroPIV system (Dantec Dynamics, Skovlunde, Denmark), consisting of an inverted fluorescence microscope Leica DMIL M LED (Leica Microsystems CMS GmbH, Wetzlar, Germany) equipped with a 10x objective, a dual-cavity Nd:YAG pulsed laser (DualPower 65-15, 532 nm, Dantec Dynamics) coupled to the microscope via a liquid light guide, and a FlowSense USB 2M-165 camera (Dantec Dynamics), Figure 2-4. The system was operated using DynamicStudio software (Dantec Dynamics).

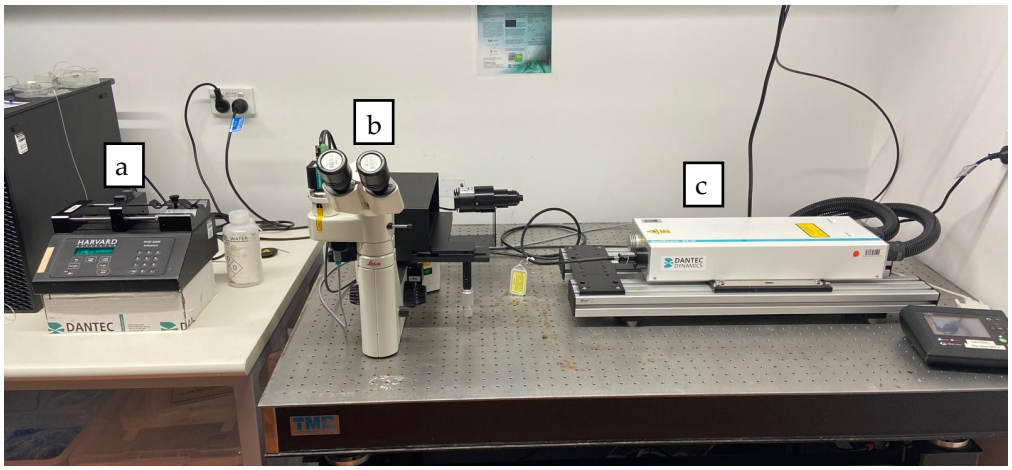

Figure 2-4: Experimental setup for micro-PIV measurements: (a) syringe pump (Harvard Apparatus) used to inject the gel sample through tubing into the microfluidic device; (b) inverted fluorescence microscope on which the device is loaded; (c) Dantec Dynamics pulse laser connected to the microscope for particle illumination.

FluoSphere carboxylate-modified fluorescent particles (1.0 µm, Nile Red 535/575 nm, Invitrogen, Thermo Fisher Scientific, Waltham, MA, USA), supplied as a 2% solids aqueous suspension, were used as seeding particles in water, HA 3% and GelMA 5% solution at a final concentration of 0.2% (v/v). The seeded solution was stirred with a tip and placed on a roller for 30 minutes to ensure homogeneous particle distribution.

Prior to each measurement all solutions were degassed under vacuum for at least 15 minutes to remove any eventual air bubbles. The final particle volume fraction was $\varphi = 4 \times 10^{-5}$ and the effect

of tracer particles on the rheology of the suspending fluid was assessed using the Einstein relation for the viscosity of a dilute suspension of rigid spheres [17]:

$$\eta = \eta_0(1+2.5\,\phi) \tag{2-1}$$

where η_0 is the viscosity of the particle-free fluid and φ is the particle volume fraction. For $\varphi = 4 \times 10^{-5}$, these yields $\eta = 1.0001\,\eta_0$, corresponding to an increase in viscosity of approximately 0.01%. The seeding particles were therefore assumed to have a negligible effect on the fluid viscosity and not to alter the measured flow. These solutions were later injected into the microfluidic device at a controlled flow rate using a syringe pump (Harvard Apparatus PHD 2000, Harvard Apparatus, Holliston, MA, USA)

2.5.2 Flow rate validation

To characterize the inlet conditions used in the simulations and verify the actual flow rate delivered by the syringe pump for a highly viscous fluid, a density measurement and a flow rate study were carried out on HA 6%, selected as the most viscous material and therefore representing the most critical case for the pump performance.

The density was determined gravimetrically: a known volume of 1 mL of solution was dispensed into a pre-weighed Petri dish, and the mass of the solution was obtained as the difference between the total mass and the empty dish mass. The measured density was 926 kg/m³, approximately 7% lower than the density of water (998.2 kg/m³). This discrepancy was attributed mainly to uncertainty in the manual volumetric measurement.

For the flow rate study, a 3-cc syringe filled with HA 6% was mounted on the syringe pump and connected to a pre-weighed Petri dish through a 20-gauge needle and tubing. After the material reached the tubing outlet, the pump was set to the target flow rate of 0.5 mL/h and started simultaneously with a timer. The accumulated mass was measured every 15 minutes over one hour, yielding four sequential measurements. After conversion to volume using the measured density, the corresponding flow rates were obtained for each interval, respectively 0.496, 0.468, 0.444, and 0.448 mL/h, with a mean value of 0.464 mL/h, corresponding to a relative error of 7.2% with respect to the imposed flow rate. This deviation was attributed to experimental uncertainty associated with handling and dispensing a highly viscous material at low flow rate and the previous error from the density measurement.

2.5.3 Measurement Protocol, image processing

Micro-PIV measurements were performed on three fluids: deionized (DI) water, used as a Newtonian reference, and the two bioinks HA 3% and GelMA 5%. These two formulations were selected as the least viscous among the characterized materials, and therefore the most experimentally manageable, since the higher viscosities of the remaining formulations could generate excessive pressures within the microfluidic device (MFD). For each fluid, three independent measurements were acquired under identical flow conditions, to assess repeatability and to obtain the mean velocity profile together with its standard deviation. Prior to each measurement, the device was primed to ensure complete wetting of the channel and removal of air bubbles. DI water was pumped through the device until the entire geometry, and the outlet reservoir were filled, after which the device was degassed under vacuum in a DI water bath for 15 minutes. The tubing was then reconnected, and additional water was flushed through to remove any residual bubbles. The device was then mounted on the micro-PIV microscope, framing a region including

section D, identified as the area of greatest interest for this study. The focal plane was set at the mid-plane of the channel to align the acquisition plane with the central region analysed in the simulations. The mid-plane was located by focusing successively on the lower and upper channel walls and positioning the focal plane at the midpoint between the two; the focus-knob travel between the two walls (15°) was consistent with the nominal channel depth (50 μm), confirming the correct identification of the wall positions. Because the micro-PIV system uses volume illumination rather than a light sheet, the whole channel depth is illuminated, and out-of-focus particles also contribute to the recorded signal. The optical depth of field (DOF), which in comparable micro-PIV configurations is only of the order of a few microns (~15 μm) describes the in-focus region but not the depth over which particles contribute to the cross-correlation. This latter quantity is the depth of measurement (or depth of correlation), δz_m given by [18]:

$$\delta z_m = \frac{3n\lambda_0}{(NA)^2} + 2.16\frac{d_p}{\tan\theta} + d_p \tag{2-2}$$

where $\theta = \sin^{-1}(NA/n)$ and the term $\frac{3n\lambda_0}{(NA)^2}$ represents the diffraction, $2.16\frac{d_p}{\tan\theta}$ geometrical-shadow and d_p finite-particle-size contributions. For the present setup (n = 1.33, λ_0 = 532 nm, NA = 0.25, d_p= 0.95 μm, θ = 10.8°), this yields δz_m = 45.6 μm, i.e. approximately 91% of the channel depth. Therefore, although the focal plane was positioned at the channel mid-plane, the measured velocity field was interpreted as representative of a depth-sampled velocity field rather than a strictly mid-plane measurement.

A calibration was first performed by acquiring a single-frame image of the geometry under white LED illumination. The channel width at section D was selected in the software and set equal to 0.6 mm, corresponding to the actual device outlet width allowing the software to associate the correct pixel-to-distance scaling. The syringe pump was then started at a flow rate of 0.32 mL/h. This value, rather than 0.5 mL/h, was used because the inlet velocity imposed in the MFD simulation (2.02×10^{-4} m/s) corresponds, for the rectangular inlet cross-section (8.8 mm × 50 μm), to a recalculated volumetric flow rate; the derivation of this inlet velocity is described in Section 2.4.3. The system was left to stabilize for approximately 5 minutes to allow the flow to reach steady-state conditions. The illumination was then switched from the white LED to the green filter for micro-PIV acquisition, and double-frame mode was selected. Images were acquired at a trigger frequency of 4 Hz, collecting 25 image pairs with a time separation between frames (Δt) of 7000 μs. To ensure reliable cross-correlation, the seeding density and the inter-frame particle displacement were controlled so that each interrogation window (64 × 64 pixels) contained approximately 10 to 25 particles, with a particle displacement of about 25% of the window size between the two frames [19]. The acquired image pairs were processed in DynamicStudio. A mask was first applied to exclude the regions outside the channel, removing spurious signal from areas not of interest. An image min/max filter was then applied, subtracting the local mean background signal from the original image to enhance particle contrast. Velocity fields were computed in DynamicStudio using the Adaptive PIV method, with interrogation window sizes ranging from 32 × 32 to 256 × 256 pixels. Spurious vectors were removed using moving-average validation and replaced by local neighbourhood averages. Temporal mean and standard deviation fields were then calculated for each velocity component.

3. Results

3.1 Rheological Characterization of Bioink Precursor

Viscosity is the fundamental rheological property quantifying a fluid's resistance to flow under shear deformation. For each bioink precursor, it was characterised by means of a steady-state shear rate sweep test, in which the applied shear rate is increased stepwise over a defined range. The resulting flow curve, viscosity as a function of shear rate, reflects the response of the material's internal microstructure to continuous shearing and is therefore representative of the conditions experienced by the bioink during extrusion-based processes such as bioprinting. It also allows to identify the constitutive law that best represents the material behaviour through curve fitting, from which the corresponding model parameters are extracted.

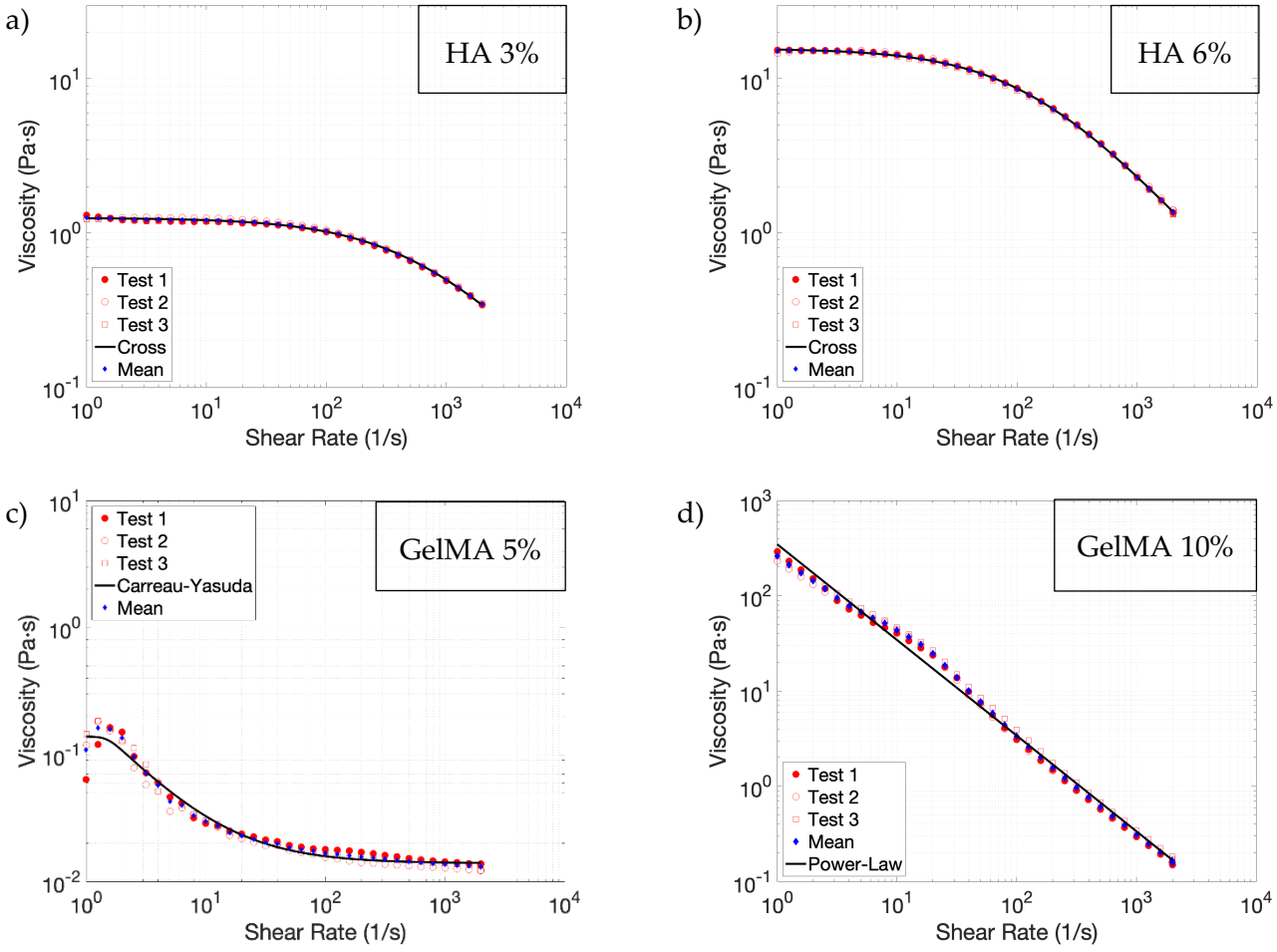

Figure 3-1: Flow curves of viscosity as a function of shear rate for (a) HA 3%, (b) HA 6%, (c) GelMA 5%, and (d) GelMA 10%, obtained from steady-state shear rate sweep measurements (Tests 1–3, shear rate range 1–2000 s^{-1}, T = 22 °C). Red markers represent experimental data from three replicates, blue diamonds indicate the mean values, and the black lines represent the fitted constitutive models: Cross (a, b), Carreau–Yasuda (c), and Power-law (d).

Figure 3-1 shows the viscosity-versus-shear-rate curves for the four bioink formulations, measured over a shear rate range of 1–2000 s^{-1} at T = 22 °C. All materials exhibit pronounced shear-thinning behaviour, with the viscosity decreasing monotonically as the shear rate increases. A high reproducibility was observed across the three replicates of each formulation, as shown by the close overlap of the individual test curves with the mean values.

The two HA formulations (Figure 3-1, a-b) display a well-defined zero-shear plateau followed by a power-law shear-thinning region, accurately captured by the simplified Cross model. HA 6% exhibits a markedly higher viscosity than HA 3% across the entire shear rate range, reflecting the denser entanglement network at higher polymer concentration. GelMA 5% (Figure 3-1, c) shows both a zero-shear and a high-shear Newtonian plateau separated by a marked shear-thinning transition, a two-plateau behaviour well described by the Carreau–Yasuda model. GelMA 10% (Figure 3-1, d), in contrast, does not display a detectable zero-shear plateau within the measured range and follows a continuous power-law decay, justifying the use of the Power-law (Ostwald–de Waele) model. As for HA, the higher-concentration formulation (GelMA 10%) is substantially more viscous than GelMA 5%. In all cases, the fitted constitutive models (solid black lines) reproduce the experimental data accurately.

The cellular formulations (vf60) of HA 3% and GelMA 5%, in contrast, follow different trends, the results are presented in Figure 3-2.

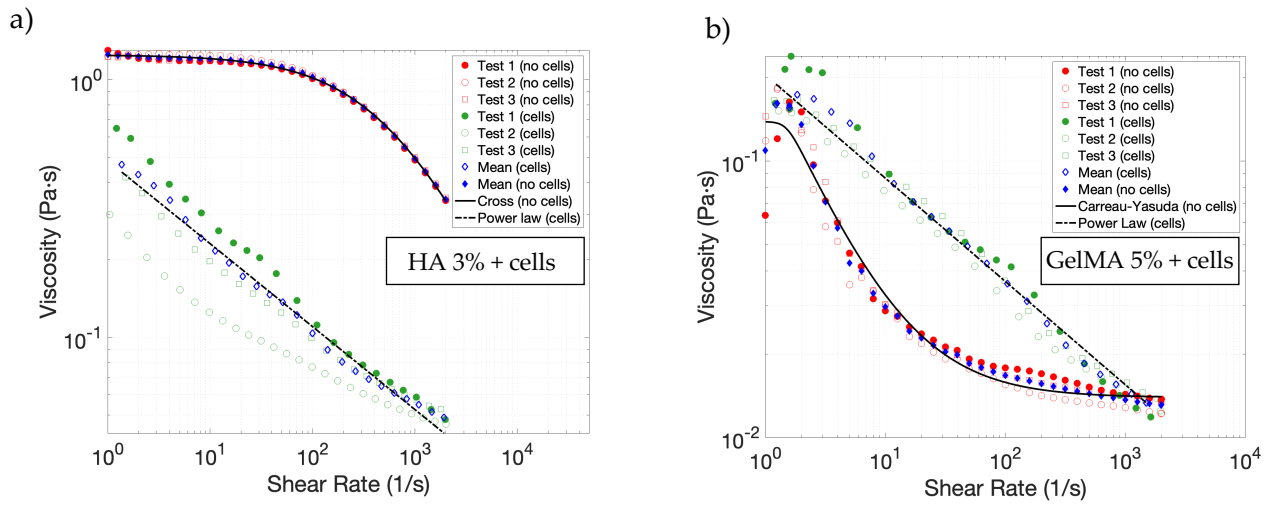

Figure 3-2: Flow curves of viscosity as a function of shear rate for (a) HA 3% and (b) GelMA 5%, from steady-state shear rate sweep measurements (Tests 1–3, 1–2000 s^{-1}, T = 22 °C). Red and green markers represent experimental data without and with cells (vf60), respectively; blue diamonds indicate mean values. Black lines show the fitted constitutive models: Cross and Carreau–Yasuda for samples without cells (solid), Power Law for samples with cells (dashed).

The flow curve of HA 3% without cells, previously described as exhibiting a well-defined zero-shear viscosity plateau and pronounced shear-thinning behaviour captured by the Cross model, undergoes a notable modification upon the addition of cells. The cellular formulation shows a systematic reduction of apparent viscosity across the full shear rate range and no longer displays a low-shear plateau, with the data better described by a Power Law; despite the viscosity reduction, the shear-thinning character is preserved. Compared to the acellular formulation, the three replicates with cells exhibit a lower degree of reproducibility, as visible from the increased scatter among the individual test curves. GelMA 5% shows an opposite trend with respect to HA 3%: the addition of cells leads to a consistent increase in apparent viscosity compared to the acellular formulation, particularly evident at low-to-intermediate shear rates. While the acellular sample is well described by the Carreau–Yasuda model, the cellular formulation, conversely, follows a Power Law behaviour without an apparent plateau; notably, at high shear rates, the two curves tend to converge towards similar viscosity values.

The constitutive model parameters obtained from the curve fitting are summarised in Table 3-1. All fitted models showed excellent agreement with the experimental data, with all coefficients of determination equal to or above $R^2 = 0.98$ (Carreau–Yasuda model, GelMA 5%).

Table 3-1: Fitted constitutive model parameters for each bioink precursor.

Material	Model	Zero-shear viscosity η_0 (Pa·s)	Infinite-shear viscosity η_∞ (Pa·s)	Relaxation time λ (s)	Power-law index n	Consistency index K (Pa·s)	Yasuda parameter a
Water	Newtonian	0.001	/	/	/	/	/
HA 3%	Cross - simplified	1.26	/	$1.68 \cdot 10^{-3}$	0.2	/	/
HA 6%	Cross - simplified	15.71	/	$7.9 \cdot 10^{-3}$	0.15	/	/
GelMA 5%	Carreau - Yasuda	0.14	$1.39 \cdot 10^{-2}$	0.66	$2.73 \cdot 10^{-14}$	/	10
GelMA 10%	Power Law	/	/	/	$-4.66 \cdot 10^{-3}$	347.93	/
HA 3% + Cells	Power Law	/	/	/	0.48	0.68	/
GelMA 5% + Cells	Power Law	/	/	/	0.20	0.63	/

To assess the flow regime within the MFD, the Reynolds number was computed at the device inlet for each fluid, Table 3-2. For each non-Newtonian material, the apparent wall shear rate at the inlet cross-section was first estimated as:

$$\dot{\gamma}_{app} = \frac{6v}{h} \tag{3-1}$$

where v is the velocity of the fluid in inlet (2.02×10^{-4} m/s), and h is the channel height (50 μm). The resulting apparent shear rate of $\dot{\gamma}_{app} = 24.24\ s^{-1}$ was then substituted into the corresponding constitutive law (Cross, Power Law or Carreau–Yasuda model) to obtain the material-specific apparent viscosity η_{app} at that shear rate. The Reynolds number was subsequently calculated as:

$$Re = \frac{\rho\, V_{rect}\, D_h}{\eta_{app}} \tag{3-2}$$

where $V_{rect} = 2.02 \times 10^{-4}$ m/s is the inlet velocity and $D_h = 99.4$ μm is the hydraulic diameter of the rectangular cross-section. For water, whose Newtonian viscosity is shear-rate independent, $\eta_{app} = 0.001$ Pa·s was used directly giving as results $Re_{rect} = 0.020$; this case is consistent with the circular geometry, since V_{rect} was itself derived by imposing Re equivalence between the rectangular and circular geometries (see Section 2.4.3). For non-Newtonian materials, the lower wall shear rate characteristic of the circular cross-section results in higher apparent viscosities and therefore even

lower Reynolds numbers, further confirming creeping flow conditions across all simulated geometries.

Table 3-2: Apparent viscosity and Reynolds number at the MFD inlet ($\dot{\gamma}_{app}$ = 24.24 s^{-1}, D_h= 99.4 µm, $V_{rect} = 2.02 \times 10^{-4}$m/s) for all tested fluids.

MFD	Water	Hyaluronic Acid 3%	Hyaluronic Acid 6%	GelMA 5%	GelMA 10%
Apparent viscosity η_{app} (Pa·s)	0.001	0.82	8.81	$2.17 \cdot 10^{-2}$	14.14
Reynolds Number (inlet)	0.02	$2.44 \cdot 10^{-5}$	$2.28 \cdot 10^{-6}$	$9.25 \cdot 10^{-4}$	$1.42 \cdot 10^{-6}$

3.2 CFD Simulations

3.2.1 Mesh Independency

A mesh independence study was performed on the 3D geometry, which features a fully independent mesh from the other two models. For the MFD model, the mesh had been previously validated by an earlier study [16], and the same cell size was therefore retained without further refinement. For the axisymmetric model, the cell dimensions were kept consistent with those of the MFD, with only minor local adjustments to reduce the maximum aspect ratio; the reliability of this mesh was instead assessed through direct comparison with the analytical Poiseuille solution for both the velocity profile and the wall shear stress, as reported in the following section.

For the 3D model, three mesh configurations were tested by selectively refining and coarsening the cell dimensions in the downstream sections of the geometry (Sections 6 - 10 in Figure 3-3), while the remaining upstream sections were kept unchanged: the medium mesh (1,730,665 elements), a finer mesh obtained by halving the cell dimensions (3,606,972 elements), and a coarser mesh obtained by doubling them (1,284,298 elements).

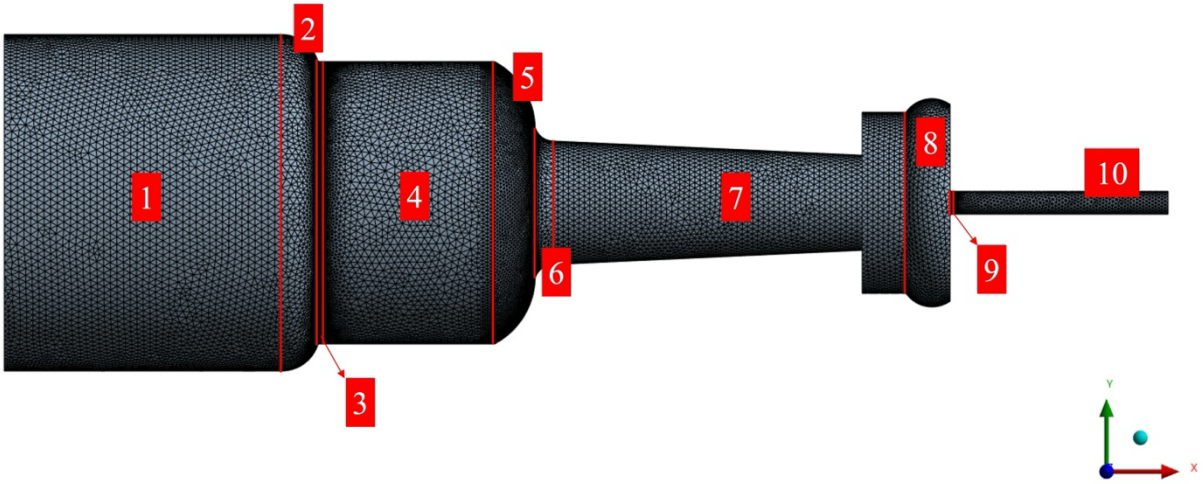

Figure 3-3: Mesh of the 3D geometry with numbered cross-sections (1–10) indicating the regions where cell dimensions were selectively refined for the mesh independence study.

Mesh quality was assessed in terms of skewness and aspect ratio. With respect to the ANSYS Fluent default skewness threshold of 0.85, the fraction of compliant elements was 90.4% for the medium mesh, 91.1% for the fine mesh, and 90.8% for the coarse mesh. Regarding aspect ratio, 99.75% of elements in the medium mesh fell below a value of 6.67, compared to 99.7% below 7.19 for the coarse mesh and 99.73% below 7.25 for the fine mesh, indicating that the medium mesh achieves the best aspect ratio quality among the three configurations. All three simulations were run under identical boundary conditions and solver settings as described in Section 2.4.3. The area-weighted outlet velocity and inlet pressure were extracted as scalar convergence metrics, together with the x-velocity profile along the y-axis at the section D. The relative error between the fine and coarse meshes was evaluated as:

$$\varepsilon = \frac{| \phi_{fine} - \phi_{coarse} |}{\phi_{fine}} \times 100\% \tag{3-3}$$

yielding values of 0.90% for the outlet velocity and 0.24% for the inlet pressure, both well below the 5% threshold commonly adopted as criterion for mesh independence. As shown in Figure 3-4 (left, centre), both quantities plateau from the medium mesh onwards, with negligible variation between the medium and fine configurations. This statement is further confirmed by the x-velocity profiles shown in Figure 3-4 (right): the fine and medium meshes are practically overlapping across the entire cross-section, while the coarse mesh underestimates the velocity values. Based on these results, the medium mesh was retained for all subsequent simulations as a suitable compromise between accuracy and computational cost.

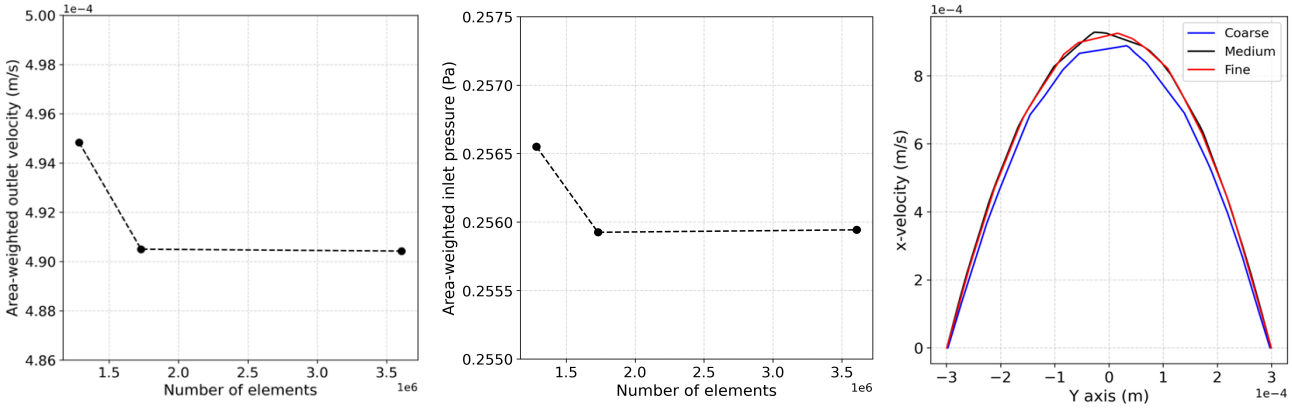

Figure 3-4: Mesh independence study results. (a) Area-weighted outlet velocity and (b) inlet pressure as a function of the number of mesh elements. (c) X-velocity profiles along the diameter for the three mesh configurations.

3.2.2 Validation Against Theoretical Poiseuille Profile

As mentioned in the mesh independence section, the validity of the axisymmetric mesh was assessed through direct comparison with the analytical Poiseuille solution and more broadly, this comparison serves as a verification step for the numerical simulations, confirming that both the axisymmetric and 3D models correctly reproduce the expected flow physics for a Newtonian fluid under the imposed boundary conditions. To this end, velocity profiles and Wall Shear Stress (WSS) distributions were extracted at four cross-sections (A, B, C, D) along the geometry for water at Q = 0.5 mL/h and compared against both the theoretical Poiseuille profiles and the corresponding 3D simulation results, as shown in Figure 3-5.

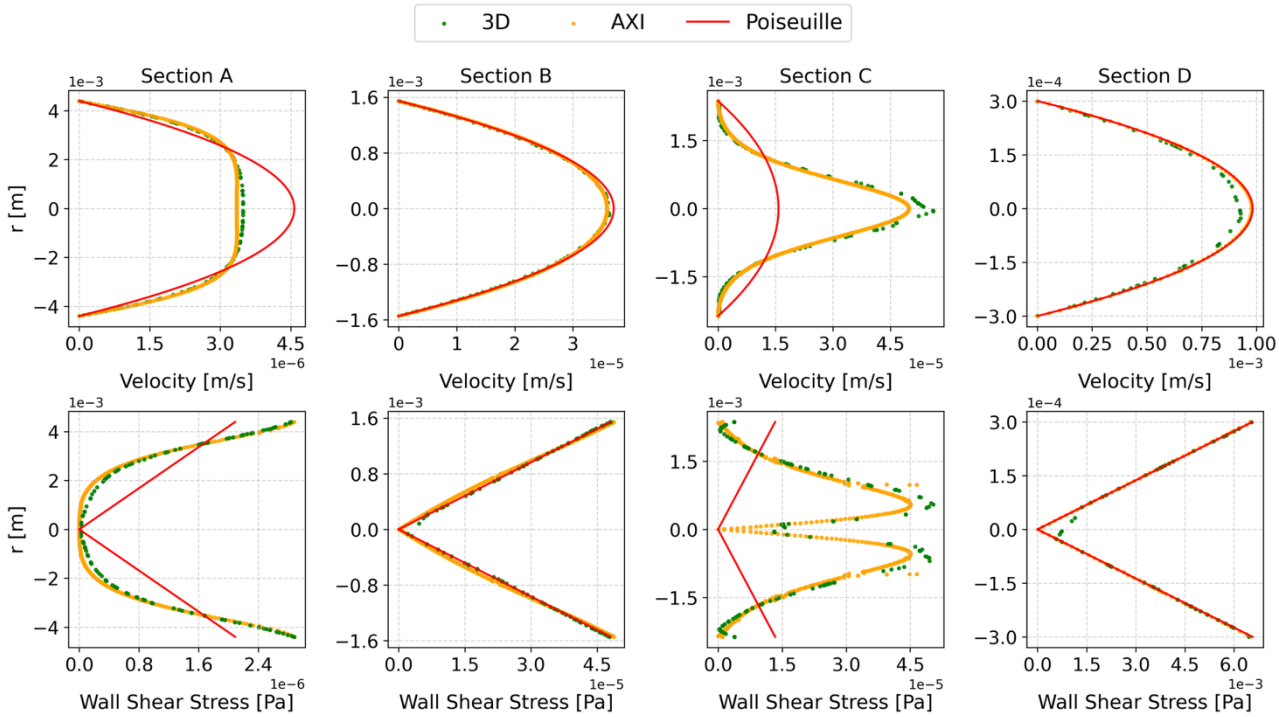

Figure 3-5: Velocity profiles (top row) and Wall Shear Stress distributions (bottom row) across four cross-sections (A, B, C, D) of the microfluidic device for water at a flow rate of 0.5 mL/h, comparing the 3D simulation, the axisymmetric (AXI) simulation, and the theoretical Poiseuille profiles. The radial coordinate r is measured from the channel axis.

At Sections B and D, both models reproduce a parabolic velocity profile in close agreement with Poiseuille theory. Section A, by contrast, shows a markedly flatter profile in both the 3D and AXI simulations, departing significantly from the Poiseuille prediction, with the velocity remaining nearly uniform across most of the cross-section before dropping steeply near the walls. This flatter profile is indicative of a not-yet-fully-developed flow, an aspect that will be examined in more detail in the Discussion Section 4.2. The axisymmetric model shows consistently closer adherence to the analytical solution across all sections, with the 3D data exhibiting slightly larger scatter. The corresponding WSS distributions at these sections follow the expected linear radial dependence, and both models align well with the theoretical profile, confirming the reliability of the mesh in regions of established flow. Section C represents a notable exception: both models deviate more markedly from the Poiseuille solution, with the 3D simulation showing the largest discrepancy, particularly in the central region of the cross-section. The WSS distribution at this section also departs from the linear trend. This behaviour is consistent with the location of Section C within a geometrical transition zone of the domain, where the assumption of fully developed flow underlying the Poiseuille solution is not satisfied. At Section D, corresponding to the outlet nozzle with the smallest cross-sectional radius (~300 μm) and highest velocities (~10^{-3} m/s), both models recover close agreement with the Poiseuille profile for both velocity and WSS, indicating that the flow has re-established a developed character at this section.

3.2.3 Comparison between Axisymmetric and 3D Results

The same comparative analysis carried out for water was repeated for all four non-Newtonian materials (HA 3%, HA 6%, GelMA 5%, and GelMA 10%) extracting velocity profiles and WSS distributions at Sections A, B, C, and D for both the 3D and axisymmetric (AXI) simulations. Figure 3-6 and Figure 3-7 show the velocity profiles and WSS distributions across Sections A–D for HA 3% and GelMA 5%, respectively; the corresponding results for HA 6% and GelMA 10% are reported in Appendix (Figure 6-1 and Figure 6-2), as they display qualitatively analogous behaviour with proportionally higher WSS magnitudes. For the materials at lower concentration, the velocity profiles at Sections A and B show good agreement between the 3D and AXI models, preserving the same qualitative shape observed for water. At Section C, a divergence between the two models is again present, consistent with what was observed in the Newtonian case. At Section D, the profiles recover a more regular shape, though the 3D data exhibit greater scatter relative to AXI. Regarding the velocity profile shape, a progressive flattening is observed compared to water, more distinct for HA 3% than for GelMA 5%, consistent with their respective apparent viscosities at the operating shear rate. The WSS distributions scale with material viscosity: HA 3% reaches maximum values of approximately 3.2×10^{-3} Pa at Section A and 8 Pa at Section D, while GelMA 5% shows significantly lower values across all sections, with a maximum of approximately 3.2×10^{-1} Pa at Section D. In both cases, the AXI model produces smoother distributions than the 3D model, with the largest divergence between the two occurring at Sections C and D.

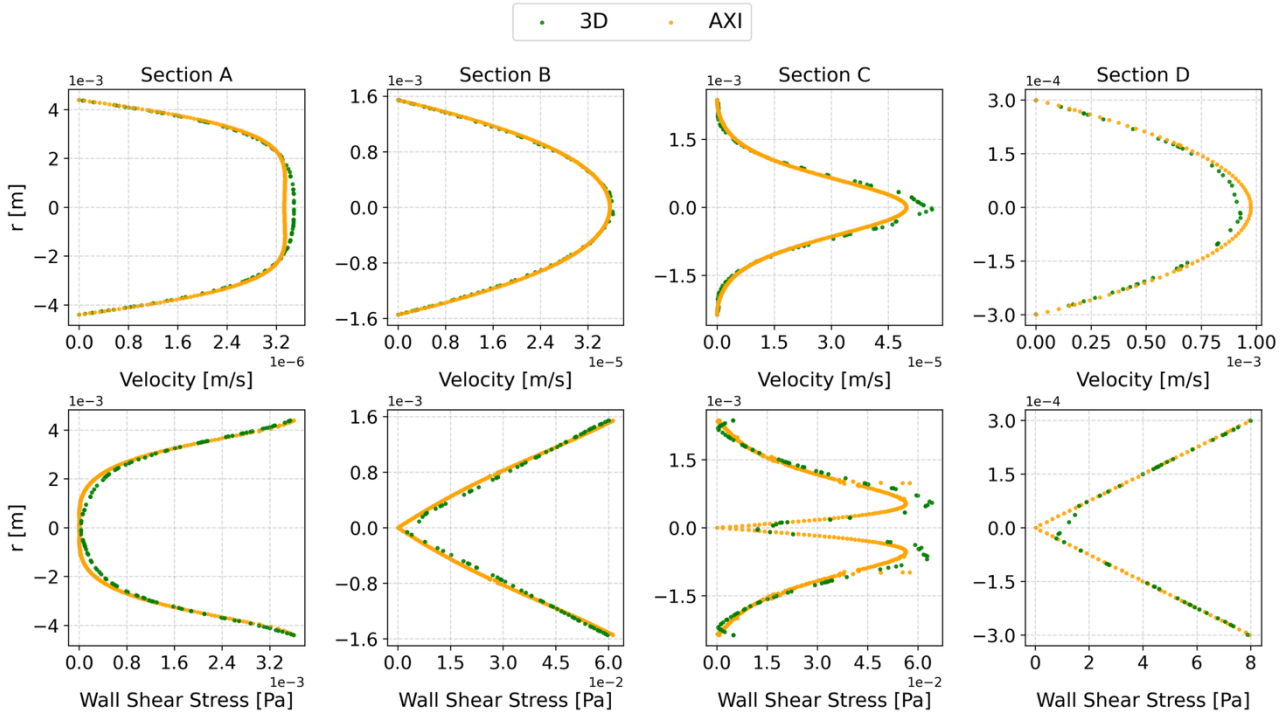

Figure 3-6: Velocity profiles (top row) and Wall Shear Stress distributions (bottom row) across four cross-sections (A, B, C, D) of the microfluidic device for HA 3% at a flow rate of 0.5 mL/h, comparing the 3D simulation, the axisymmetric (AXI) simulation. The radial coordinate r is measured from the channel axis.

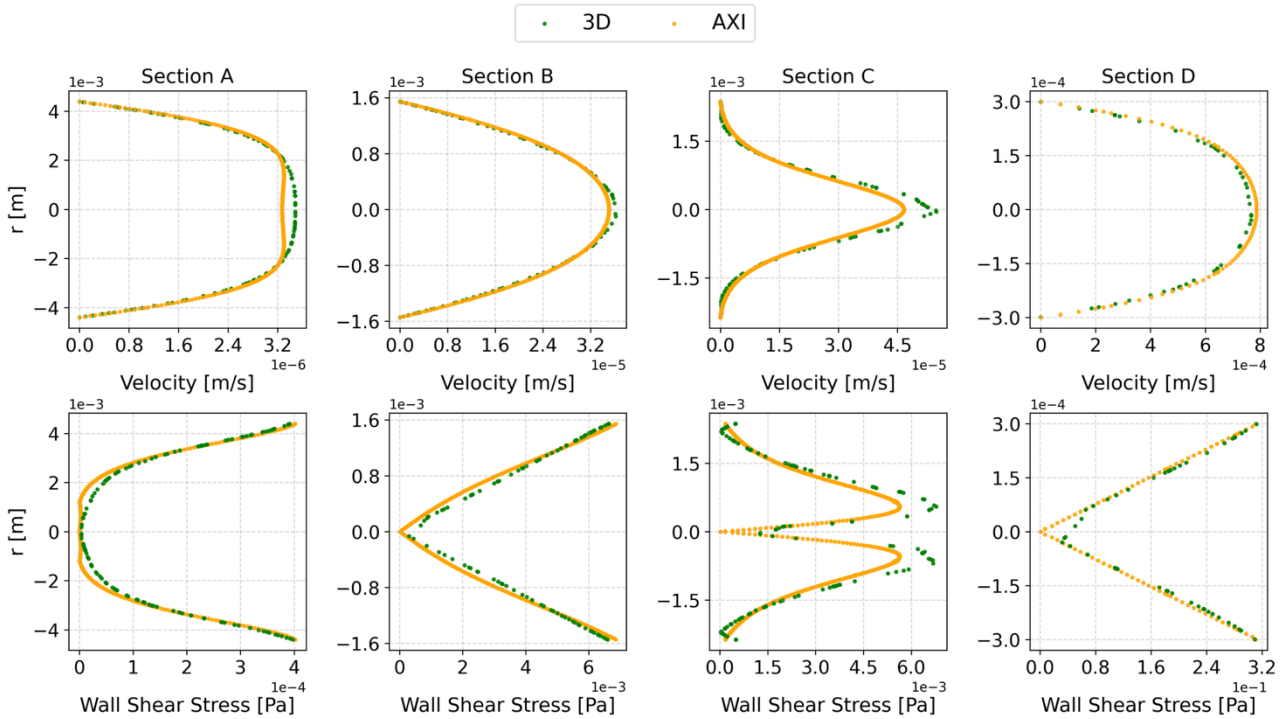

Figure 3-7: Velocity profiles (top row) and Wall Shear Stress distributions (bottom row) across four cross-sections (A, B, C, D) of the microfluidic device for GelMA 5% at a flow rate of 0.5 mL/h, comparing the 3D simulation, the axisymmetric (AXI) simulation. The radial coordinate r is measured from the channel axis.

The results for HA 6% and GelMA 10%, reported in Appendix 6. (Figure 6-1 and Figure 6-2), show qualitatively the same behaviour described above. At Sections A and B, the 3D and AXI models are

in good agreement, while Section C displays the same divergence pattern observed for all other materials. At Section D, the 3D data show increased scatter relative to AXI, with the divergence being particularly marked for GelMA 10%. The velocity profiles of HA 6% are qualitatively similar to those of HA 3% across all sections, with comparable peak velocity values. GelMA 10% shows the most pronounced profile flattening among all tested materials, with a peak velocity at Section D of approximately 6×10^{-4} m/s, the lowest recorded across the full material set. The WSS magnitudes for HA 6% and GelMA 10% are substantially higher than those of their lower-concentration counterparts. At Section D, HA 6% and GelMA 10% both reach values on the order of 10^{2} Pa, representing the highest WSS values observed across all simulated materials and sections. At Section A, HA 6% shows a maximum WSS of approximately 4.5×10^{-2} Pa, while GelMA 10% reaches approximately 8×10^{-1} Pa, both significantly exceeding the corresponding values for HA 3% and GelMA 5%.

3.3 Comparison Between CFD Simulations and Micro-PIV Experimental Measurements

Micro-PIV measurements were performed at an imposed flow rate of Q = 0.32 mL/h, corresponding to the inlet velocity used in the MFD CFD simulations. Each of the three tests was conducted using a different physical device, cleaned and reassembled independently before each acquisition, to account for device-to-device variability. Measurements were carried out at the section D approximately, on water HA 3%, and GelMA 5%, selected as the three materials with the lowest apparent viscosity among those investigated.

The CFD simulation for water produces a peaked velocity profile with a maximum of 4.63×10^{-3} m/s at the channel centreline. The three PIV tests show a qualitatively similar shape, with a mean peak velocity of 4.68×10^{-3} m/s, yielding a relative error of 0.97% with respect to the CFD peak. The RMSE between the mean PIV profile and the CFD profile is 5.32×10^{-4} m/s, corresponding to 11.5% of the CFD peak velocity, Figure 3-8. The standard deviation band is relatively narrow, indicating good inter-device reproducibility. The plug region width, defined as the central zone where velocity exceeds 95% of the peak, measures 0.49 mm in the CFD and 0.31 mm in the mean PIV profile.

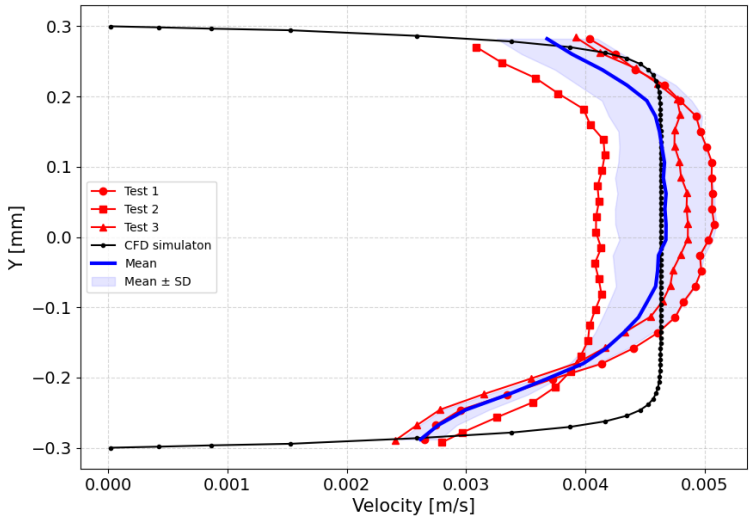

Figure 3-8: Velocity profiles obtained with water at an imposed flow rate of 0.32 mL/h. The red curves represent the experimental measurements acquired by micro-PIV (Tests 1–3), the blue curve represents the mean experimental profile, and the shaded blue area indicates the standard deviation. The black curve corresponds to the CFD simulation results.

The CFD profile for HA 3% displays a markedly flatter shape compared to water, with a broad central plateau and steep velocity gradients near the walls, characteristic of plug-like flow behaviour in a shear-thinning fluid. Nevertheless, only limited agreement is observed in the peak region with the PIV tests, while differences in the profile shape remain evident, Figure 3-9; the peak velocity is 4.74×10^{-3} m/s, deviating from the CFD value of 4.50×10^{-3} m/s by 5.39%, and an RMSE of 6.58×10^{-4} m/s, corresponding to 14.6% of the CFD peak velocity. In this case the plug region width is 0.48 mm in the CFD profile and 0.18 mm in the mean PIV profile.

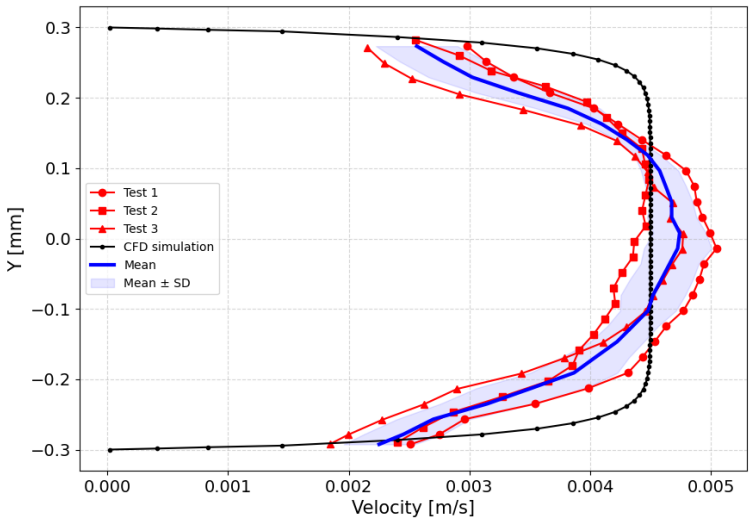

Figure 3-9: Velocity profiles obtained with HA 3% at an imposed flow rate of 0.32 mL/h. The red curves represent the experimental measurements acquired by micro-PIV (Tests 1–3), the blue curve represents the mean experimental profile, and the shaded blue area indicates the standard deviation. The black curve corresponds to the CFD simulation results.

For GelMA 5% the CFD profiles show a shape closely comparable to that of water, consistent with its relatively low apparent viscosity among the non-Newtonian materials tested. The PIV tests display the largest inter-device variability among all three materials, with individual profiles deviating substantially from one another and a markedly wider standard deviation band than for both water and HA 3%, Figure 3-10. The mean experimental profile peaks at 4.54×10^{-3} m/s, with a relative error of 0.73% with respect to the CFD peak of 4.51×10^{-3} m/s, and an RMSE of 6.73×10^{-4} m/s, corresponding to 14.9% of the CFD peak velocity. For the CFD the plug region width measures 0.49 mm and 0.20 mm for the mean PIV profile. The relative errors on the peak velocity across all three materials, ranging from 0.73% to 5.39%, are consistent with the velocity deviations reported in comparable micro-PIV and CFD validation studies in microfluidic devices, where deviations within 5% of the mean flow velocity have been documented [20].

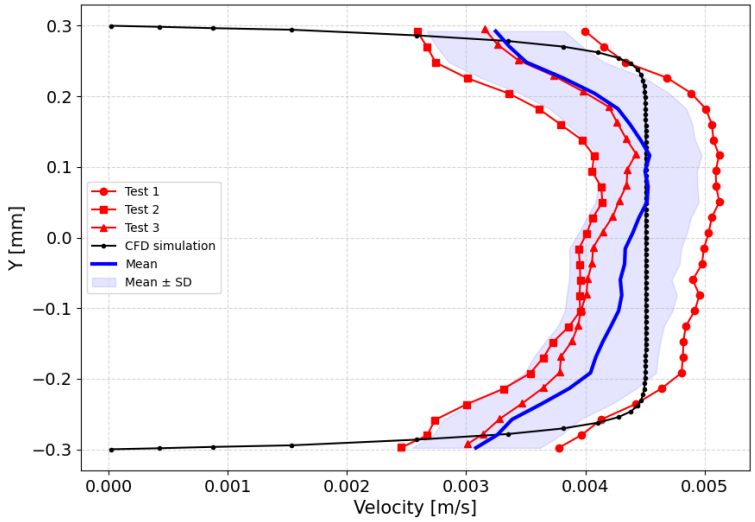

Figure 3-10: Velocity profiles obtained with GelMA 5% at an imposed flow rate of 0.32 mL/h. The red curves represent the experimental measurements acquired by micro-PIV (Tests 1–3), the blue curve represents the mean experimental profile, and the shaded blue area indicates the standard deviation. The black curve corresponds to the CFD simulation results.

4. Discussion

4.1 Rheological behaviour of bioink precursor

All materials investigated (HA 3%, HA 6%, GelMA 5% and GelMA 10%) exhibit shear-thinning behaviour over the shear rate range tested, with viscosity decreasing monotonically as shear rate increases. This pseudoplastic response is a key rheological requirement for extrusion-based bioprinting: under the high shear rates experienced within the nozzle, the material viscosity drops markedly, facilitating extrusion; once deposited, the network structure recovers, supporting shape retention [21, 22]. Despite sharing this common flow behaviour, the two material families differ substantially in the physical mechanism underlying it, Figure 3-1.

In the HA formulations, shear-thinning arises from the progressive disruption of physical entanglements and non-covalent interactions between hyaluronic acid chains under flow. At rest, the high-molecular-weight HA chains adopt a two-fold helical conformation stabilised by intramolecular hydrogen bonds involving carboxylic, amide, and hydroxyl groups, together with water bridges between neighbouring sugar residues [23], forming an entangled network that confers high zero-shear viscosity. Above the entanglement concentration of 1 mg/mL, a threshold well exceeded by HA 3% at 30 mg/mL, inter-chain interactions further contribute to the formation of a transient three-dimensional network [24], whose viscoelastic properties are largely independent of temperature under physiological conditions [23]. As the shear rate increases, chains progressively align along the flow direction, reducing entanglement density and inter-chain interactions, and viscosity decreases accordingly. The more pronounced shear-thinning behaviour and higher zero-shear viscosity of HA 6% relative to HA 3% reflects the denser entanglement network formed at higher polymer concentration [21]. The shear-thinning behaviour of GelMA formulations derives from a distinct physical mechanism. GelMA is a collagen-derived polypeptide whose chains undergo a thermo-reversible coil-to-helix transition upon cooling: characteristic Gly-Pro-Hyp repeating sequences promote the formation of collagen-like triple-helix junction zones stabilised by

hydrogen bonding, building a physically crosslinked network [25]. In warm water (≥ 40°C), chains exist as denatured, flexible coiled polypeptides; upon cooling below the sol-gel transition temperature, which is 22.6 °C for GelMA 5%, physical gelation occurs through the partial reformation of these triple helices [26]. At 22°C, GelMA 5% is at or near its sol-gel transition temperature but, in the absence of UV-induced covalent crosslinking, does not establish a consolidated three-dimensional network, behaving instead as a weakly structured viscoelastic fluid. Under shear, the applied mechanical stress progressively disrupts the already limited triple-helix junction zones, reducing network connectivity and therefore viscosity, already low and close to that of water. The more marked shear-thinning and higher viscosity of GelMA 10% relative to GelMA 5% reflect the denser triple-helix network formed at higher concentration, which presents a greater number of junction zones susceptible to shear-induced disruption and an increase of the sol-gel transition temperature, specifically 25.9 °C [25, 26].

Cell-laden formulations tested on just two of the gels, HA 3% and GelMA 5%, exhibited greater inter-replicate variability compared to their acellular counterparts, as evidenced by the wider spread of individual test curves in Figure 3-2. This is attributed to the inherent heterogeneity of biological suspensions, in which the cellular aggregation state may vary between replicates: at high volume fraction, adhesive cell–cell attractions promote flocculation, and the resulting cluster size and distribution are sensitive to the sample preparation pathway and timeframe [27]. The incorporation of NIH 3T3 cells at high volume fraction (vf60) produced opposite effects on the rheological behaviour of the two bioink families, as shown in Figure 3-2.

The addition of cells to the HA 3% formulation resulted in a decrease in viscosity across the measured shear rate range. For hydrogel-based bioinks at moderate-to-high polymer concentrations, cell incorporation has generally been shown to reduce viscosity across a range of systems, including alginate-gelatin and silk fibroin-gelatin bioinks [9, 28]. No studies were found reporting this effect specifically for HA-based bioinks; however, the underlying mechanism is considered analogous, as both alginate and HA form concentration-dependent physical networks sustained by inter-chain interactions and non-covalent crosslinks in the absence of covalent crosslinking agents. The governing mechanism has not been conclusively established, but the most plausible explanation is that cells physically disrupt the inter-chain interactions sustaining the polymer network, blocking the non-covalent crosslinks that maintain the gel structure and thereby reducing the bulk viscosity of the suspension [9, 28]. This interpretation is consistent with findings by Schwartz et al. [29], who reported a similar decline in viscosity and yield stress with increasing cell density, attributed to cells causing blockage of inter-chain interactions within the polymeric blend. Contrasting results were reported by Xu et al. [30], who observed increased viscosity with increasing cell concentration; this discrepancy was attributed by Majumder et al. to the dilute nature of the alginate system used by Xu et al. compared to concentrated bioinks, highlighting that the presence or absence of a pre-existing polymer network is the key determinant of the direction of the rheological response to cell incorporation. In contrast with the HA, and in line with the behaviour reported by Xu et al. [30] for dilute polymer systems, the incorporation of cells into GelMA 5% resulted in a measurable increase in viscosity. At 22°C and without UV crosslinking, GelMA 5% does not form a consolidated network structure, as previously explained, and cells therefore act as discrete particulate inclusions that increase resistance to flow, in a manner analogous to the Einstein model for dilute suspensions [10].The absence of a pre-existing polymer network places GelMA 5% in the concentration regime where particulate effects dominate over network disruption effects, accounting for the observed viscosity increase upon cell addition.

4.2 Comparison Between Axisymmetric and 3D Approaches

The velocity and WSS profiles obtained from the 3D and axisymmetric (AXI) simulations show good agreement across all four cross-sections (A–D), confirming that the axisymmetric simplification captures the essential flow physics of the circular-section geometry. The 3D simulation shows slightly larger point-to-point scatter, particularly in the WSS distributions; this is attributed to the greater mesh complexity of the 3D geometry: a higher total element counts with less regular element shapes introduce larger local discretization errors, producing small deviations from the smooth trends captured by the structured axisymmetric mesh.

For the case of water (Figure 3-5), a theoretical Poiseuille profile is included as an additional reference with the Newtonian case. Agreement with the Poiseuille solution is observed in Sections B and D, where the flow is fully developed within straight channel segments of sufficient length. In Section A, located approximately 2 mm from the device inlet, the velocity profile retains a more plug-like shape rather than a parabolic one. This is consistent with the hydrodynamic entry length predicted by the correlation of Durst et al. [31] for low-Reynolds-number pipe flows:

$$\frac{L_h}{D} = [(0.619)^{1.6} + (0.0567 \cdot Re)^{1.6}]^{1/1.6} \tag{4-1}$$

which, for the water case at the inlet Reynolds number of this geometry, yields an entry length of approximately 5.5 mm, considerably longer than the 2 mm distance at which Section A is located. The flow has therefore not yet reached a fully developed state at that cross-section, moreover the flow simulated in this work is steady and viscous, therefore governed by elliptic equations. A fundamental property of elliptic problems is that disturbances propagate in all directions, including upstream [12]. As a result, the presence of the downstream constriction alters the flow field upstream of the geometric discontinuity itself and so the fluid begins to reorganize its velocity profile before it is physically encountered. This was further confirmed by auxiliary simulations comparing a straight cylinder of equivalent dimensions with and without the downstream constriction: in the unconstrained geometry, a fully developed parabolic profile was recovered at approximately 5.5 mm from the inlet, following the previously equation, while in the geometry with the constriction, the velocity profile never stabilized in the upstream region. In Section C, located at the onset of the geometric expansion, a further departure from the Poiseuille profile is observed, of a different nature from that in Section A. The upstream influence of the expansion prevents the formation of a locally fully developed profile: the fluid at the centreline retains the momentum acquired in the upstream narrow channel, while the fluid in the peripheral region finds itself adjacent to a receded wall and has not yet adapted to the new boundary conditions. This results in a peaked inner profile and a nearly stagnant outer region, with WSS approaching zero at the peripheral zone and reaching its maximum at the boundary between the two regions.

For both non-Newtonian fluids (Figure 3-6 and Figure 3-7), it is possible to notice the same plug-like shape retained at Section A and a more developed profile visible at Section B. In the Section C the same behaviour of water is observed for HA 3% and GelMA 5%, confirming that the distortion of the velocity profile is primarily governed by the geometry of the expansion rather than by the rheological properties of the fluid. A key difference between the two fluids is visible in the WSS distributions. HA 3%, being significantly more viscous than GelMA 5% across the measured shear rate range, produces substantially higher WSS values at all cross-sections. Most markedly at Section D, the WSS for HA 3% reaches values on the order of 8 Pa, compared to 3.2×10^{-1} Pa for GelMA 5%

and 6×10^{-3} Pa for water. This reflects the direct dependence of wall shear stress on fluid viscosity at a given flow rate and is consistent with the rheological characterization results.

4.3 Comparison between CFD and Micro-PIV

CFD simulations were performed in ANSYS Fluent on the MFD geometry and compared with the micro-PIV experimental measurements. Velocity profiles were extracted at section D, which corresponds to a straight rectangular channel segment. The CFD results were obtained in both the XY plane (top view, transverse direction along the channel width) and the ZY plane (side view, along the channel height), while micro-PIV measurements were limited to the XY plane at the focal plane corresponding to the channel mid-height (Z = 25 μm). In the ZY plane, the CFD predicts the expected parabolic velocity profile along the channel height, as shown from Figure 6-3 to Figure 6-6, in the Appendix. In the XY plane, however, the CFD predicts a plug-like profile along the channel width for all tested fluids. This behaviour reflects the geometry of the rectangular cross-section, which presents an aspect ratio of W/H = 12: in such conditions, the lateral velocity profile in the XY plane is substantially flattened in the central region, away from the lateral walls. This stands in contrast to what is observed in square microchannels, where an aspect ratio close to unity produces a parabolic profile in both transverse directions, as reported by Fu et al. [32] for Newtonian fluids.

The micro-PIV measurements were limited to the XY plane; for water (Figure 3-8), as a Newtonian reference fluid, the experimental profiles (Tests 1–3) show a qualitative agreement with the plug-like shape predicted by the CFD and consistent with the channel geometry, in line with the micro-PIV validation reported by Rodd et al. [14] in PDMS rectangular microchannels of comparable dimensions. However, some deviations from an ideal plug-flow profile are observed. First, the experimental velocity does not reach zero at the lateral walls, as would be expected from the no-slip boundary condition. This is likely attributable to the finite size of the PIV interrogation windows: the cross-correlation algorithm averages the displacement over an area that spans several micrometres, so that near-wall interrogation regions simultaneously capture stationary particles at the wall and slower-moving particles slightly away from it, resulting in a non-zero averaged velocity at the wall. Second, a mild asymmetry is visible between the positive and negative Y sides of the profile, which may be attributed to a slight misalignment of the devices with respect to the focal plane, or to the presence of a particle or minor obstructions near one of the lateral walls during acquisition.

For the hyaluronic acid 3% solution (Figure 3-9), the CFD model predicts a velocity profile that is even more plug-like than that observed for water. This expectation is physically grounded: in a shear-thinning fluid, the apparent viscosity decreases with increasing shear rate. Since shear rate is highest near the lateral walls, the fluid in those regions becomes locally less viscous and flows more easily, while the central region, where shear rate is low, retains a higher apparent viscosity, producing a profile that is flatter than the parabolic Newtonian case. The experimental micro-PIV measurements for HA 3%, however, deviate substantially from this expectation, showing a curved, approximately parabolic shape with a pronounced central peak. Several alternative explanations were considered and found unlikely: a misalignment of the measurement plane, lateral wall slip and device-to-device geometric variability are similarly improbable given the consistency of results across the different devices tested. A more compelling explanation emerges from a direct observation made during image acquisition. Unlike the measurements performed with water and GelMA 5%, in which individual fluorescent beads appeared as isolated sub-micrometre spots, the raw micro-PIV images acquired with HA 3% showed the presence of markedly larger bright

features, suggesting the formation of multi-particle aggregates. Two physicochemical mechanisms may account for this. First, depletion aggregation: non-adsorbing polymer chains are entropically excluded from the gap between approaching particles, generating an osmotic pressure imbalance that drives them together, a mechanism documented for hyaluronic acid as a depletant acting on negatively charged biological particles [33]. Second, cation-mediated bridging: the divalent cations present in cDMEM (Ca2+, Mg2+) can simultaneously coordinate carboxylate groups on the bead surface and on the HA chain, effectively bridging the two, a mechanism well established for anionic polymer–particle systems in the presence of multivalent ions [34]. No further characterisation of the aggregation mechanism was performed within the scope of this work. Regardless of the underlying cause, the presence of these larger aggregates may have influenced the micro-PIV measurements in two ways: they may have responded differently to the local velocity field due to their greater size and inertia, or they may have been misidentified by the cross-correlation algorithm, which assumes tracer particles of uniform sub-micrometre size, leading to erroneous velocity vectors. In either case, the apparent parabolic shape of the HA 3% profile is likely an artefact of tracer aggregation rather than a genuine feature of the flow, and the CFD prediction of a plug-like profile is considered more physically reliable for this fluid.

For GelMA 5% (Figure 3-10), the CFD predicts a plug-like velocity profile consistent with the channel geometry and the shear-thinning rheology of the material, analogous to the expectation described for HA 3%. The experimental micro-PIV measurements confirm this plug-like shape, with the mean profile showing reasonable qualitative agreement with the CFD prediction. However, the three individual test profiles exhibit considerably higher inter-replicate variability than observed for water, with each test showing a distinct shape, including lateral asymmetries and shifted velocity peaks, resulting in a wide standard deviation band around the mean. This variability it may be attributed to minor imperfections in the fabricated devices, such as slight deviations in channel width or cross-sectional uniformity across independently manufactured replicates, or to the presence of small debris or air inclusions near the channel walls that locally perturb the flow or partially obstruct the optical path during acquisition. Notably, no anomalous tracer behaviour comparable to that observed in HA 3% was detected during GelMA 5% acquisitions, suggesting that the variability here is of geometric or experimental origin rather than related to tracer-fluid interactions.

5. Conclusion

This work pursued the rheological characterisation of HA and GelMA bioink precursors, in the absence and in the presence of encapsulated cells, together with the development and quantitative experimental validation of a CFD model of a microfluidic device (MFD) mimicking a bioprinting nozzle. All four acellular formulations (HA 3%, HA 6%, GelMA 5%, and GelMA 10%) were shown to exhibit pronounced shear-thinning behaviour, well captured by the Cross, Carreau–Yasuda, and Power-law constitutive models, with the underlying physical mechanism differing between the two material families. The incorporation of NIH 3T3 cells at high volume fraction (vf60) revealed opposite rheological responses for the two materials: a decrease in viscosity for HA 3%, consistent with cells disrupting a pre-existing concentrated polymer network, and an increase in viscosity for GelMA 5%, consistent with cells acting as discrete particulate inclusions in a dilute, structurally weak system. This contrast confirmed that the direction of the rheological response to cell incorporation is governed by the presence or absence of a consolidated polymer network at the working concentration, rather than by cell content alone.

The CFD models developed for the MFD, axisymmetric, and 3D geometries showed good agreement between the axisymmetric and 3D approaches across all tested materials, and were validated against the analytical Poiseuille solution for water at sections away from geometric transitions. The quantitative comparison with micro-PIV measurements for the MFD geometry, performed on water, HA 3%, and GelMA 5%, confirmed the reliability of the CFD predictions for water and GelMA 5%, with peak-velocity relative errors below 1%. For HA 3%, the micro-PIV measurements deviated substantially from the CFD-predicted plug-like profile, an effect attributed to tracer particle aggregation specific to this fluid rather than to a limitation of the computational model itself, which is considered to remain the more physically reliable description of the underlying flow.

Taken together, these results show that a consistent rheological-computational-experimental pipeline can be applied to both acellular and cell-laden shear-thinning bioinks, with the constitutive parameters and CFD predictions adapting to the specific formulation under study, while the quantitative validation against micro-PIV remains, at present, restricted to the acellular case for which direct optical access to the flow field was experimentally feasible.

Several aspects remain open for future investigation. HA 6% and GelMA 10% were rheologically characterised in this work but not included in the micro-PIV validation, as their higher viscosity made them less experimentally manageable within the MFD; extending the quantitative validation to these higher-concentration formulations would help establish whether the agreement observed for the less viscous materials holds across the full concentration range investigated. Extending micro-PIV validation to the cell-laden formulations represents a further, distinct methodological challenge, since it would require tracking the cells themselves rather than the inert tracer particles used in this work. A possible direction would be to fluorescently label the cell nucleus to track its trajectory within the flow field, while separately labelling the cell membrane to quantify cell deformation under flow via fluorescence microscopy; combined with the quantitative velocity data already established for the acellular case, this would provide a progressively more detailed and material-specific picture of how cells themselves respond to the flow, complementing rather than replacing the bulk velocity validation performed in this work.

Beyond the specific results obtained, this work also contributes to the field on a more methodological level. Quantitative CFD validation against direct flow-field measurements remains comparatively uncommon in extrusion-based bioprinting research, where qualitative approaches such as streak imaging are more frequently used; the micro-PIV comparison performed here therefore provides a reproducible, numerically verifiable benchmark for the specific MFD geometry and bioink precursors considered. At the same time, the identification of tracer particle aggregation in HA 3% represents a cautionary methodological finding in its own right: it shows that standard micro-PIV seeding particles, while well suited to water and GelMA 5%, cannot be assumed to behave inertly in all hydrogel precursors, and that an unexpected deviation between CFD and experimental data does not necessarily indicate a flaw in the computational model. Overall, this work provides a coherent rheological and fluid-dynamic characterisation of conventional shear-thinning bioinks, showing that rheology and flow behaviour cannot be fully understood in isolation when cells are involved; closing this gap, by extending the same quantitative rigour to cell-laden systems, remains the natural next step.

6. Appendix

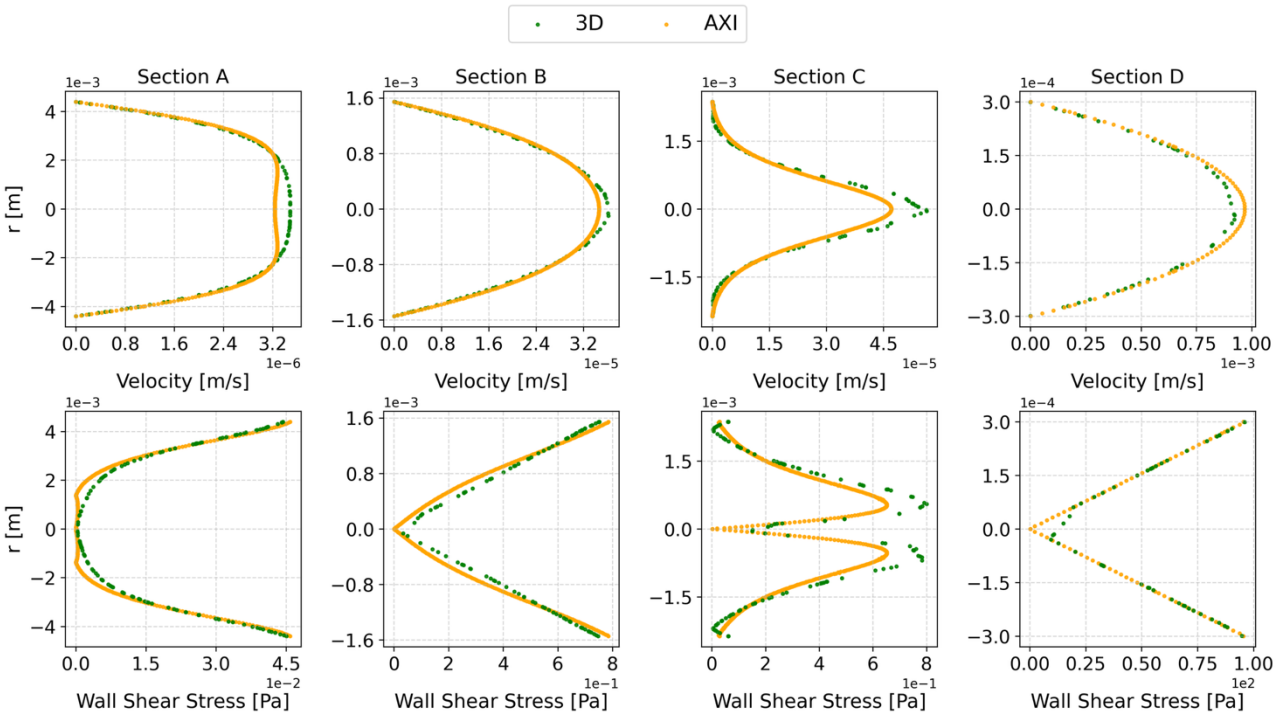

Figure 6-1: Velocity profiles (top row) and Wall Shear Stress distributions (bottom row) across four cross-sections (A, B, C, D) of the microfluidic device for HA 6% at a flow rate of 0.5 mL/h, comparing the 3D simulation, the axisymmetric (AXI) simulation. The radial coordinate r is measured from the channel axis.

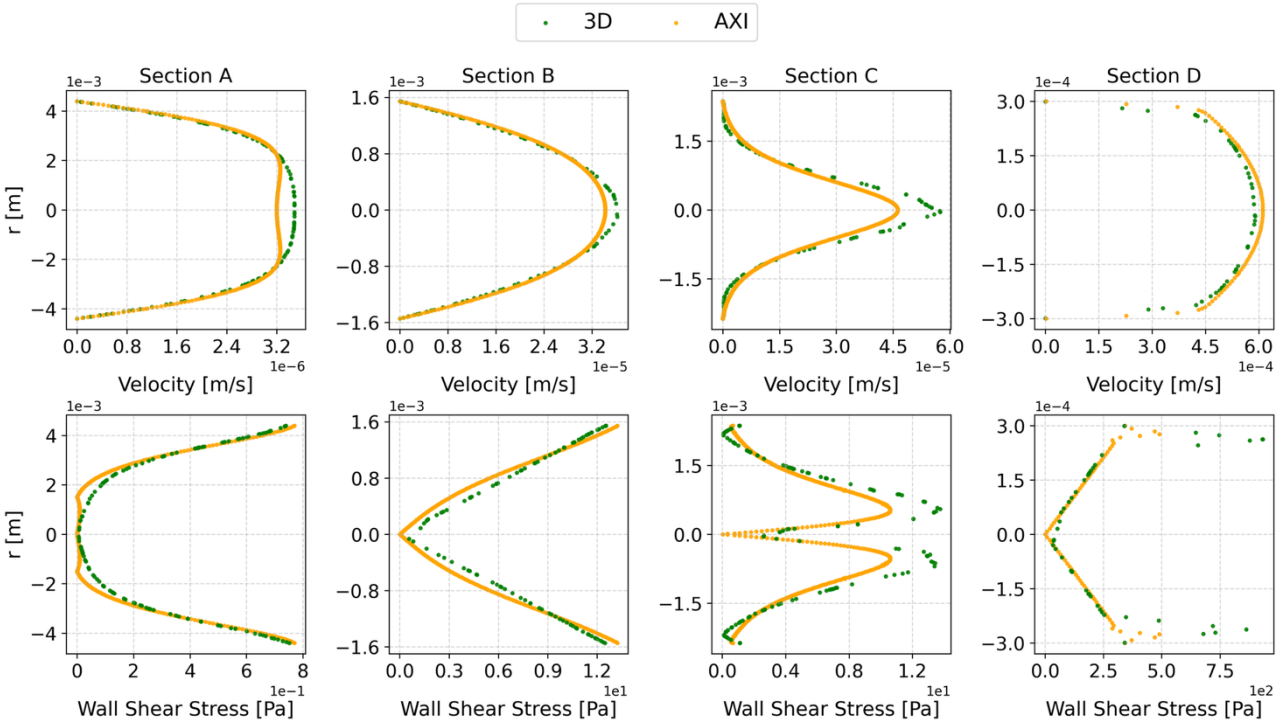

Figure 6-2: Velocity profiles (top row) and Wall Shear Stress distributions (bottom row) across four cross-sections (A, B, C, D) of the microfluidic device for GelMA 10% at a flow rate of 0.5 mL/h, comparing the 3D simulation, the axisymmetric (AXI) simulation. The radial coordinate r is measured from the channel axis

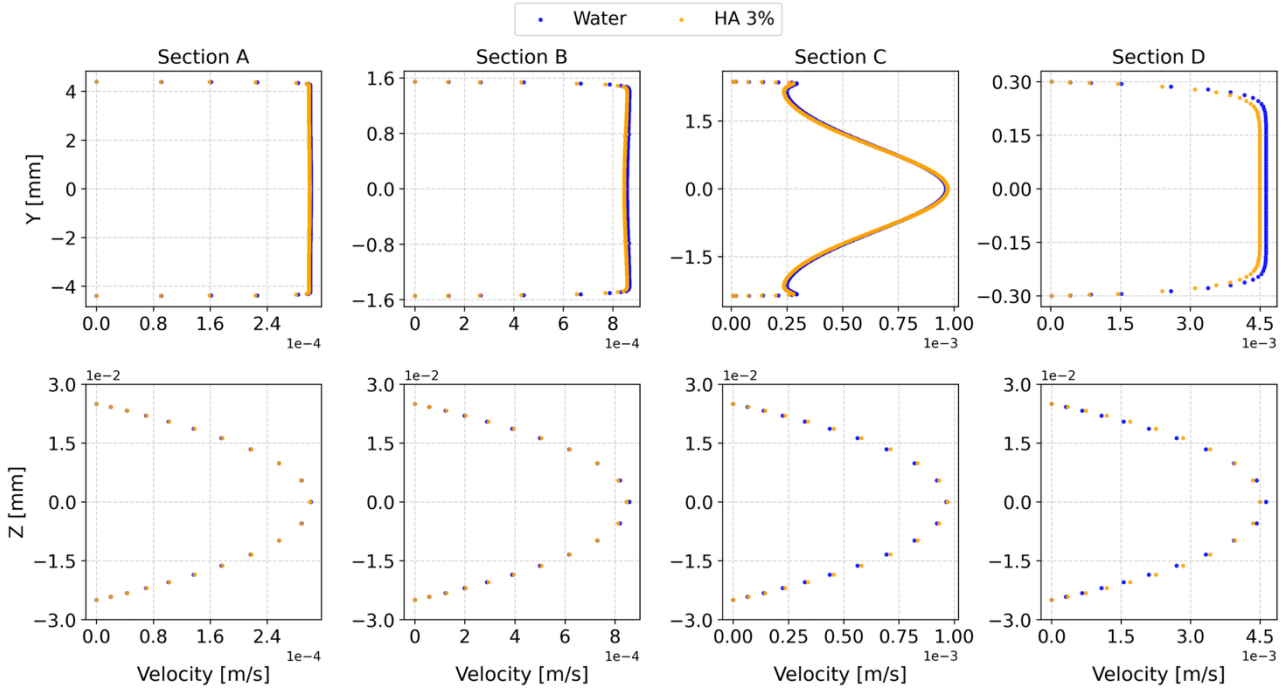

Figure 6-3: Velocity profiles across four cross-sections (A, B, C, D) of the microfluidic device for Water and HA 3% in cDMEM at a flow rate of 0.5 mL/h. The upper row shows velocity profiles along the width of the device (Y direction), while the lower row shows profiles along the height of the device (Z direction). Each profile is mirrored about the channel axis to reconstruct the full cross-sectional distribution.

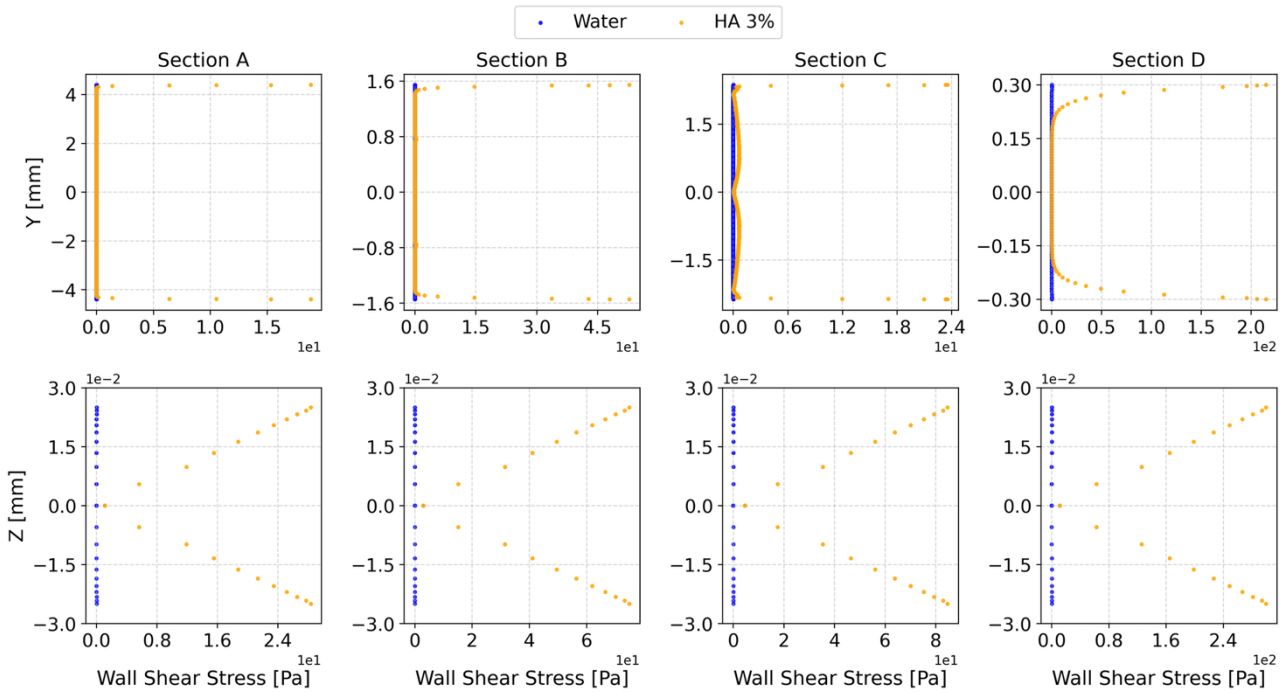

Figure 6-4: Wall Shear Stress distribution across four cross-sections (A, B, C, D) of the microfluidic device for Water and HA 3% in cDMEM at a flow rate of 0.5 mL/h. The upper row shows velocity profiles along the width of the device (Y direction), while the lower row shows profiles along the height of the device (Z direction). Each profile is mirrored about the channel axis to reconstruct the full cross-sectional distribution.

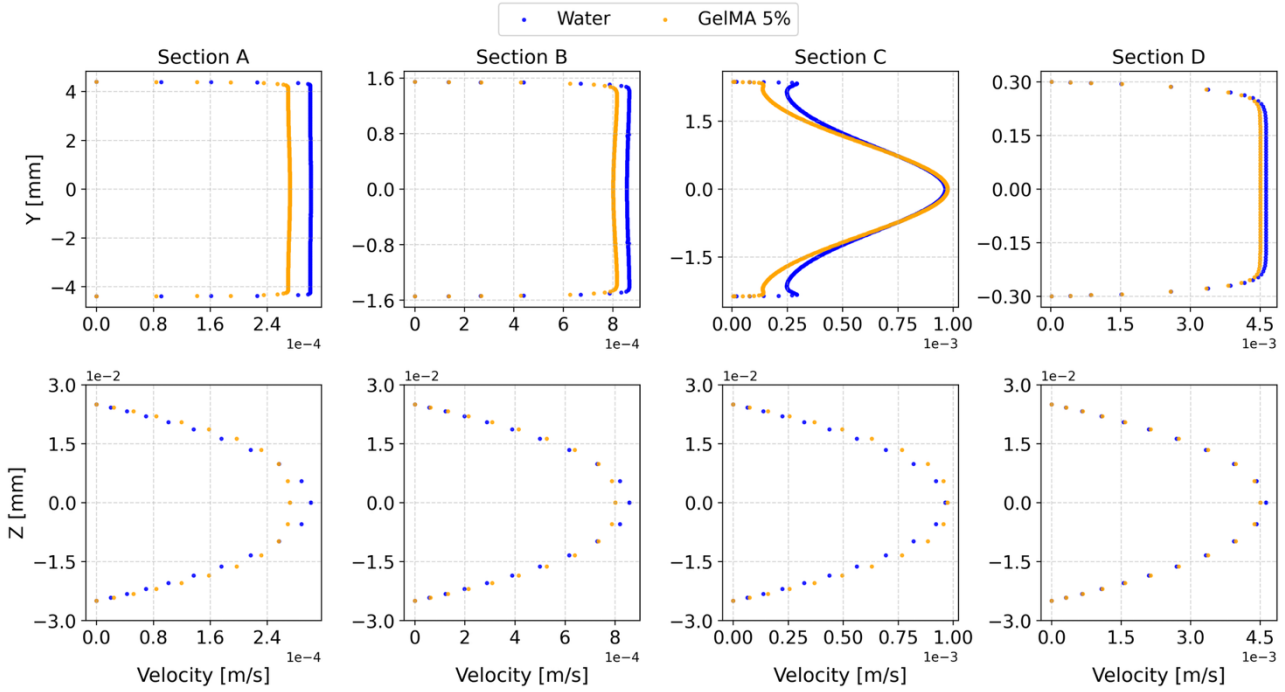

Figure 6-5: Velocity profiles across four cross-sections (A, B, C, D) of the microfluidic device for Water, GelMA 5% in cDMEM at a flow rate of 0.5 mL/h. The upper row shows velocity profiles along the width of the device (Y direction), while the lower row shows profiles along the height of the device (Z direction). Each profile is mirrored about the channel axis to reconstruct the full cross-sectional distribution

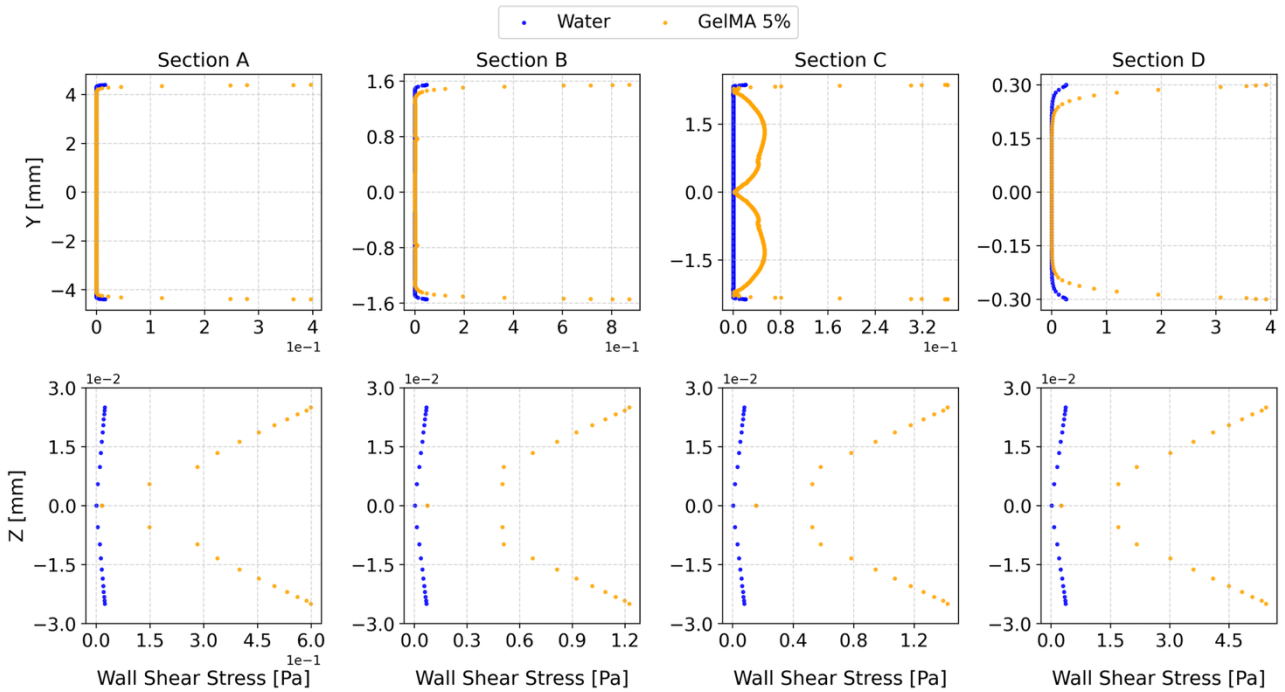

Figure 6-6: Wall Shear Stress distribution across four cross-sections (A, B, C, D) of the microfluidic device for Water and GelMA 5% in cDMEM at a flow rate of 0.5 mL/h. The upper row shows velocity profiles along the width of the device (Y direction), while the lower row shows profiles along the height of the device (Z direction). Each profile is mirrored about the channel axis to reconstruct the full cross-sectional distribution.

Acknowledgment

First and foremost, I would like to thank Professor Bozzi and Professor Redaelli for giving me the chance to be part of this project, and Professor Justin Cooper-White for welcoming me into his research team at the University of Queensland. Working under their supervision has been a true opportunity to grow, both scientifically and personally. I am also thankful to the team of the Chemical Engineering Department at UQ, whose help and presence made even the most demanding moments of this work easier to face.

Bibliography

1. Foundation, E.I., *Annual Report 2024 – Highlights*. 2024: Leiden, The Netherlands.
2. Persaud, A., et al., *3D bioprinting with live cells.* Engineered Regeneration, 2022. **3**(3): p. 292-309.
3. Antony Jose, S., A. Evtimow, and P.L. Menezes, *Advances in 3D Bioprinting: Materials, Processes, and Emerging Applications.* Micromachines, 2026. **17**(3): p. 282.
4. Dey, M. and I.T. Ozbolat, *3D bioprinting of cells, tissues and organs.* Scientific reports, 2020. **10**(1): p. 14023.
5. Gungor-Ozkerim, P.S., et al., *Bioinks for 3D bioprinting: an overview.* Biomaterials science, 2018. **6**(5): p. 915-946.
6. Lam, E.H.Y., et al., *3D bioprinting for next-generation personalized medicine.* International journal of molecular sciences, 2023. **24**(7): p. 6357.
7. Ning, L., et al., *Characterization of cell damage and proliferative ability during and after bioprinting.* ACS Biomaterials Science & Engineering, 2018. **4**(11): p. 3906-3918.
8. Xu, H.-Q., et al., *A review on cell damage, viability, and functionality during 3D bioprinting.* Military Medical Research, 2022. **9**(1): p. 70.
9. Majumder, N., A. Mishra, and S. Ghosh, *Effect of varying cell densities on the rheological properties of the bioink.* Bioprinting, 2022. **28**: p. e00241.
10. Diamantides, N., et al., *High density cell seeding affects the rheology and printability of collagen bioinks.* Biofabrication, 2019. **11**(4): p. 045016.
11. Mezger, T., *The rheology handbook: for users of rotational and oscillatory rheometers*. 2020: European Coatings.
12. Ferziger, J.H., M. Perić, and R.L. Street, *Computational methods for fluid dynamics*. Vol. 3. 2002: Springer.
13. Fareez, U.N.M., et al., *Computational Fluid Dynamics (CFD) Analysis of Bioprinting.* Advanced Healthcare Materials, 2024. **13**(20): p. 2400643.
14. Rodd, L.E., et al., *Role of the elasticity number in the entry flow of dilute polymer solutions in micro-fabricated contraction geometries.* Journal of Non-Newtonian Fluid Mechanics, 2007. **143**(2): p. 170-191.
15. Dynamics, D. *Measurement principles of PIV*. Particle Image Velocimetry (PIV) – Solutions in Fluid Mechanics 2026 June 2026]; Available from:

https://www.dantecdynamics.com/solutions/fluid-mechanics/particle-image-velocimetry-piv/measurement-principles-of-piv/.

16. FLOCCO, A., *Rheological characterization of common bioink precursors and CFD simulation of bioink flow in microfluidic models of bioprinting nozzles.* 2024.
17. Arrhenius, S., *The Viscosity of Solutions.* Biochem J, 1917. **11**(2): p. 112-33.
18. Meinhart, C.D., S.T. Wereley, and M. Gray, *Volume illumination for two-dimensional particle image velocimetry.* Measurement Science and Technology, 2000. **11**(6): p. 809-814.
19. Dynamics, D. *DynamicStudio software help (context-sensitive documentation)*. 2025.
20. Bown, M.R., et al., *Three-dimensional, three-component velocity measurements using stereoscopic micro-PIV and PTV.* Measurement Science and Technology, 2006. **17**(8): p. 2175.
21. Sekar, M.P., et al., *Hyaluronic Acid as Bioink and Hydrogel Scaffolds for Tissue Engineering Applications.* ACS Biomaterials Science & Engineering, 2023. **9**(6): p. 3134-3159.
22. Yin, J., et al., *3D Bioprinting of Low-Concentration Cell-Laden Gelatin Methacrylate (GelMA) Bioinks with a Two-Step Cross-linking Strategy.* ACS Applied Materials & Interfaces, 2018. **10**(8): p. 6849-6857.
23. Kadam, Y., et al., *Viscoelastic Behaviors of Hyaluronic Derivatives as a Function of pH, Salt, and Temperature.* Journal of Polymer Science, 2026. **64**(6): p. 1505-1517.
24. Jacoboni, I., et al., *Hyaluronic Acid by Atomic Force Microscopy.* Journal of Structural Biology, 1999. **126**(1): p. 52-58.
25. Van Den Bulcke, A.I., et al., *Structural and Rheological Properties of Methacrylamide Modified Gelatin Hydrogels.* Biomacromolecules, 2000. **1**(1): p. 31-38.
26. Das, S., J.T. Jegadeesan, and B. Basu, *Gelatin Methacryloyl (GelMA)-Based Biomaterial Inks: Process Science for 3D/4D Printing and Current Status.* Biomacromolecules, 2024. **25**(4): p. 2156-2221.
27. Maisonneuve, B.G.C., et al., *Effects of Synthetic Biomacromolecule Addition on the Flow Behavior of Concentrated Mesenchymal Cell Suspensions.* Biomacromolecules, 2015. **16**(1): p. 275-283.
28. Gregory, T., et al., *Rheological characterization of cell-laden alginate-gelatin hydrogels for 3D biofabrication.* Journal of the Mechanical Behavior of Biomedical Materials, 2022. **136**: p. 105474.
29. Schwartz, R., et al., *Cell encapsulation in gelatin bioink impairs 3D bioprinting resolution.* J Mech Behav Biomed Mater, 2020. **103**: p. 103524.
30. Xu, C., et al., *Study of Droplet Formation Process during Drop-on-Demand Inkjetting of Living Cell-Laden Bioink.* Langmuir, 2014. **30**(30): p. 9130-9138.
31. Durst, F., et al., *The Development Lengths of Laminar Pipe and Channel Flows.* Journal of Fluids Engineering, 2005. **127**(6): p. 1154-1160.
32. Fu, T., et al., *Newtonian and Non-Newtonian Flows in Microchannels: Inline Rheological Characterization.* Chemical Engineering & Technology, 2016. **39**(5): p. 987-992.
33. Weinhofer, A.C., et al., *Reversible Bacterial Depletion Aggregation and Restabilization by Water-Soluble Polymers.* Langmuir, 2025. **41**(41): p. 28109-28118.

34. Vajihinejad, V., et al., *Water Soluble Polymer Flocculants: Synthesis, Characterization, and Performance Assessment.* Macromolecular Materials and Engineering, 2019. **304**(2): p. 1800526.